Chemotrophy-based phosphatic microstromatolites from the Mississippian at Drewer, Rhenish Massif, Germany

Jennifer Zwicker[1], Daniel Smrzka[2], Matthias Gothieu[2], Eugen Libowitzky[1], Michael M. Joachimski[3] ⦿, Michael Ernst Böttcher[4,5,6] and Jörn Peckmann[7] ⦿

[1]Institut für Mineralogie und Kristallographie, Universität Wien, Wien, Austria; [2]Fachbereich Geowissenschaften, Universität Bremen, Bremen, Germany; [3]GeoZentrum Nordbayern, Friedrich-Alexander Universität Erlangen-Nürnberg (FAU), Erlangen, Germany; [4]Geochemie & Isotopen-Biogeochemie, Leibniz-Institut für Ostseeforschung (IOW), Warnemünde, Germany; [5]Marine Geochemie, Universität Greifswald, Greifswald, Germany; [6]Interdisziplinäre Fakultät, Department für Maritime Systeme, Universität Rostock, Rostock, Germany and [7]Institut für Geologie, Centrum für Erdsystemforschung und Nachhaltigkeit, Universität Hamburg, Hamburg, Germany

Abstract

The Drewer quarry located in the Rhenish Massif is a well-studied outcrop that comprises Upper Devonian (Famennian) to Lower Carboniferous (Viséan) strata. Within the Drewer deposits two black shale intervals have been described that are linked to two global oceanic anoxic events, the Hangenberg Event and the Lower Alum Shale Event. The black shales associated with the Middle Tournaisian Lower Alum Shale Event contain abundant phosphatic concretions, which were investigated using thin section petrography, powder X-ray diffraction, Fourier-transform infrared spectrometry and scanning electron microscopy. The concretions formed during several growth phases under anoxic and at least episodically sulphidic conditions within the sediment and served as a substrate for subsurface microbial mats that formed phosphatic microstromatolites. The microstromatolites occur either as partially branched columns of up to 600 μm in length attached to the phosphatic concretions or as smaller, bulbous aggregates surrounding the concretions. Element mapping identified the presence of pyrite and other metal sulphides within the phosphatic microstromatolites. The carbon and oxygen stable isotopic composition of phosphate-associated carbonate within the phosphatic microstromatolites suggests that the mat-forming microorganisms were probably anaerobic, chemotrophic microbial communities dwelling in the anoxic environment during the Lower Alum Shale Event. Such interpretation agrees with the deeper-water depositional setting of the Lower Alum Black Shale and its high content of organic matter, suggesting that chemotrophic microbial mats are potent agents of phosphogenesis in general, and of the formation of phosphatic stromatolites in particular.

CAMBRIDGE
UNIVERSITY PRESS

1. Introduction

Black shales are organic-rich sediments that commonly formed coevally in space and time through Earth history and have been associated with perturbations in the carbon cycle, climate change and global extinction events (Schlanger & Jenkyns, 1976; Arthur & Sagemann, 1994; Sagemann *et al.* 2003; Jenkyns, 2010). They are characterized by rapid and efficient accumulation of organic matter in marine sediments, either by increased primary production or efficient preservation. Black shales commonly contain phosphorus-rich rocks referred to as phosphorites, which are defined by P_2O_5 contents of 18 wt.% or higher (Föllmi, 1996). Phosphorites and black shales require similar formation conditions and are therefore commonly encountered together in the rock record. Phosphogenesis, which describes the precipitation of authigenic phosphorus minerals in marine sediments, occurs within a specific environmental spectrum where ocean circulation, sedimentation and the preservation of organic matter during early diagenesis allow for phosphorus to accumulate sufficiently in sedimentary pore waters (Glenn *et al.* 1994; Föllmi, 1996; Benitez-Nelson, 2000; März *et al.* 2008; Küster-Heins *et al.* 2010). In the modern ocean, such conditions exist in suboxic to anoxic marine sediments typified by a constant supply of organic matter, as observed in coastal upwelling zones, continental margin sediments or restricted marine basins (Filipelli & Delaney, 1996; Schenau *et al.* 2000; Filipelli, 2011; Lomnitz *et al.* 2016). Because phosphorus is highly mobile and is cycled efficiently during early diagenesis, persistent anoxic conditions are required to allow for phosphorus minerals to precipitate (Ruttenberg & Berner, 1993; Ingall & Jahnke, 1994; Föllmi, 1996; Kraal *et al.* 2012). Phosphogenesis typically requires multiple phosphorus sources including the anaerobic microbial degradation of organic matter, the reductive dissolution of iron oxides releasing adsorbed phosphate, as well as the degradation and dissolution of bone

material and fish debris (Jensen *et al.* 1995; Schenau *et al.* 2000; Smith *et al.* 2015). Since phosphorus minerals such as carbonate fluorapatite are common in organic-rich black shales, these deposits are regarded as type sections for phosphogenesis that hold important clues on the driving processes enabling the formation of sedimentary phosphate minerals (Filippelli, 2011).

Phosphatic stromatolites have been found in Proterozoic and Phanerozoic carbonate, phosphorite and black shale lithologies (Krajewski *et al.* 2000; Caird *et al.* 2017; Sallstedt *et al.* 2018; Zoss *et al.* 2019). Stromatolites are lithified microbial build-ups that are the result of the interaction between various microbial metabolic processes and their sedimentary environment (Dupraz & Visscher, 2005; Allwood *et al.* 2007; Sallstedt *et al.* 2018). Stromatolites in the fossil record have commonly been interpreted as products of cyanobacteria due to their remarkable similarity to modern cyanobacterial mats (Stal, 2012). A cyanobacterial origin has also been suggested for phosphatic stromatolites, occurring in shallow marine settings due to the presence of preserved oxygen gas bubbles (Bosak *et al.* 2009; Sallstedt *et al.* 2018), laminated fabrics related to trapping and binding mechanisms, stable isotope analyses, mineralogy, as well as facies analyses of the host sediments (Rao *et al.* 2000, 2002; Lundberg & McFarlane, 2011; Drummond *et al.* 2015; Caird *et al.* 2017; Sallstedt *et al.* 2018). Modern examples of such cyanobacterial phosphatic stromatolites are scarce and have only recently been described from a low-phosphorus terrestrial environment (Büttner *et al.* 2021). In contrast to these photosynthesis-based cyanobacterial stromatolites, phosphogenesis can result from organic matter degradation by anaerobic, sulphate-reducing bacteria (Thamdrup & Canfield, 1996; Benitez-Nelson, 2000; Arning *et al.* 2009a; Berndmeyer *et al.* 2012). A further relationship between bacteria involved in the sulphur cycle and phosphogenesis has been suggested for various ancient and modern phosphorite and phosphorus-rich deposits (Williams & Reimers, 1983; Schulz & Schulz, 2005; Bailey *et al.* 2007, 2013; Arning *et al.* 2009a; Cosmidis *et al.* 2013; Zwicker *et al.* 2021), in particular with regard to the large, colourless chemotrophic sulphide-oxidizing bacteria. These bacteria take up and release phosphate into the pore waters during early diagenesis and are capable of storing polyphosphate within their cells (Schulz & Schulz, 2005; Sievert *et al.* 2007; Zopfi *et al.* 2008; Goldhammer *et al.* 2010).

Here we report chemotrophy-based phosphatic microstromatolites enclosed in black shales deposited after the Devonian–Carboniferous transition in the course of the globally coeval, transgressive Lower Alum Shale Event (Sobolev *et al.* 2000; Siegmund *et al.* 2002; Kaiser *et al.* 2011; Becker *et al.* 2016, 2021). These black shales are rich in phosphorous concretions that host phosphatic microstromatolites of various size and morphology. Using a comprehensive approach combining petrography, mineralogy and isotope geochemistry, it is suggested that the stromatolite-forming microbial communities thrived in deep-water environments and were independent of sunlight but relied on chemotrophic metabolic pathways.

2. Geological setting and locality

2.a. Tectonic setting

The Rhenohercynian Basin is part of the Avalonian Plate and was related to numerous active subduction zones associated to the closing Rheic Ocean (Oncken *et al.* 2000). The Rhenohercynian

fold and thrust belt, which comprises the Rhenish Massif, are part of the Middle European Variscides that occur as well exposed and complete Middle Devonian to Lower Carboniferous successions (Oncken *et al.* 1999). The Rhenohercynian Zone has been characterized as an evolving rift system developing on Upper Devonian to Lower Carboniferous subsiding shelf sediments of the Old Red Continent (von Raumer *et al.* 2017). This zone, along with the Saxothuringian and the Moldanubian zones, divides the Central European Variscides from the northwest to the southeast (Kossmat, 1927; Brinkmann, 1948). The Rhenish Massif has been associated with the Avalonian Terrain that separated from Gondwana in the Early Ordovician (Oncken *et al.* 2000; Eckelmann *et al.* 2014). The resulting Rheic Ocean began to close in the Early Devonian up to the Carboniferous and involved the formation of several microplates separating the closing ocean from the Paleotethys and the Rhenohercynian Ocean by island arcs, which accreted to Avalonia in the Early Devonian (Oncken & Weber, 1995). The opening of the Rhenohercynian Ocean has been related to an active Laurussian continental margin that separated the Avalonian terranes (von Raumer & Stampfli, 2008; Zeh & Gerdes, 2010). These island arcs are documented by rocks of the Mid-German Rise, or 'Mid-German Crystalline Zone' (Altenberger *et al.* 1990; Dombrowski *et al.* 1995), which separates the Rhenohercynian from the Saxothuringian zones (Zeh & Gerdes, 2010).

The Rhenohercynian Basin developed as an elongated, narrow trough between the Mid-German Rise to the south and the London-Brabant High in the north as part of the Old Red Continent during the Middle Devonian (Königshof *et al.* 2016). The Upper Devonian sedimentary rocks of the Rhenohercynian Basin are part of the Hercynian Facies that comprise siltstones and red shales, reef carbonates and bioherms and drowned carbonate platforms (Becker *et al.* 2016). The Late Devonian reefs were subject to several global extinction events such as the Kellwasser crisis in the latest Frasnian and the Hangenberg Event at the Devonian–Carboniferous boundary (Becker *et al.* 2016). Deposits of the lowermost Carboniferous in the Rhenish Massif comprise cherts, organic-rich black shales and turbiditic limestones, which have been collectively associated with the 'Kulm-Facies'. In the Early Carboniferous, the Rhenohercynian Basin was successively closed and subducted under the Mid-German High, forming an active continental margin as evidenced by extensive local volcanism (Oncken & Weber, 1995; Siegmund *et al.* 2002).

2.b. Upper Devonian to Mississippian strata at Drewer

The Drewer quarry represents the northernmost locality of the Rhenish Massif cropping out within several anticlinal and synclinal structures (Becker *et al.* 2016), which are part of a larger thrust and fold belt with numerous synclinal and anticlinal systems from the Velbert and Remscheid-Altena anticlines to the west and the larger Warstein anticline to the south (Fig. 1). Drewer is located within the Belecke anticline, which formed an intrabasinal swell in a starved basin during the Early Carboniferous (Clausen *et al.* 1989; Korn, 2010). It represents a key lithostratigraphic and biostratigraphic locality for the Devonian–Carboniferous boundary displaying Milankovich cyclicity, several regressions and transgressions, as well as extinction events as recorded by the Hangenberg and Lower Alum Shale Events (Becker, 1992, 1999; Korn *et al.* 1994; Siegmund *et al.* 2002; Kumpan *et al.* 2015; Becker *et al.* 2016). These two black shale intervals have been correlated globally to coeval strata in Spain, France and Poland, as well as to
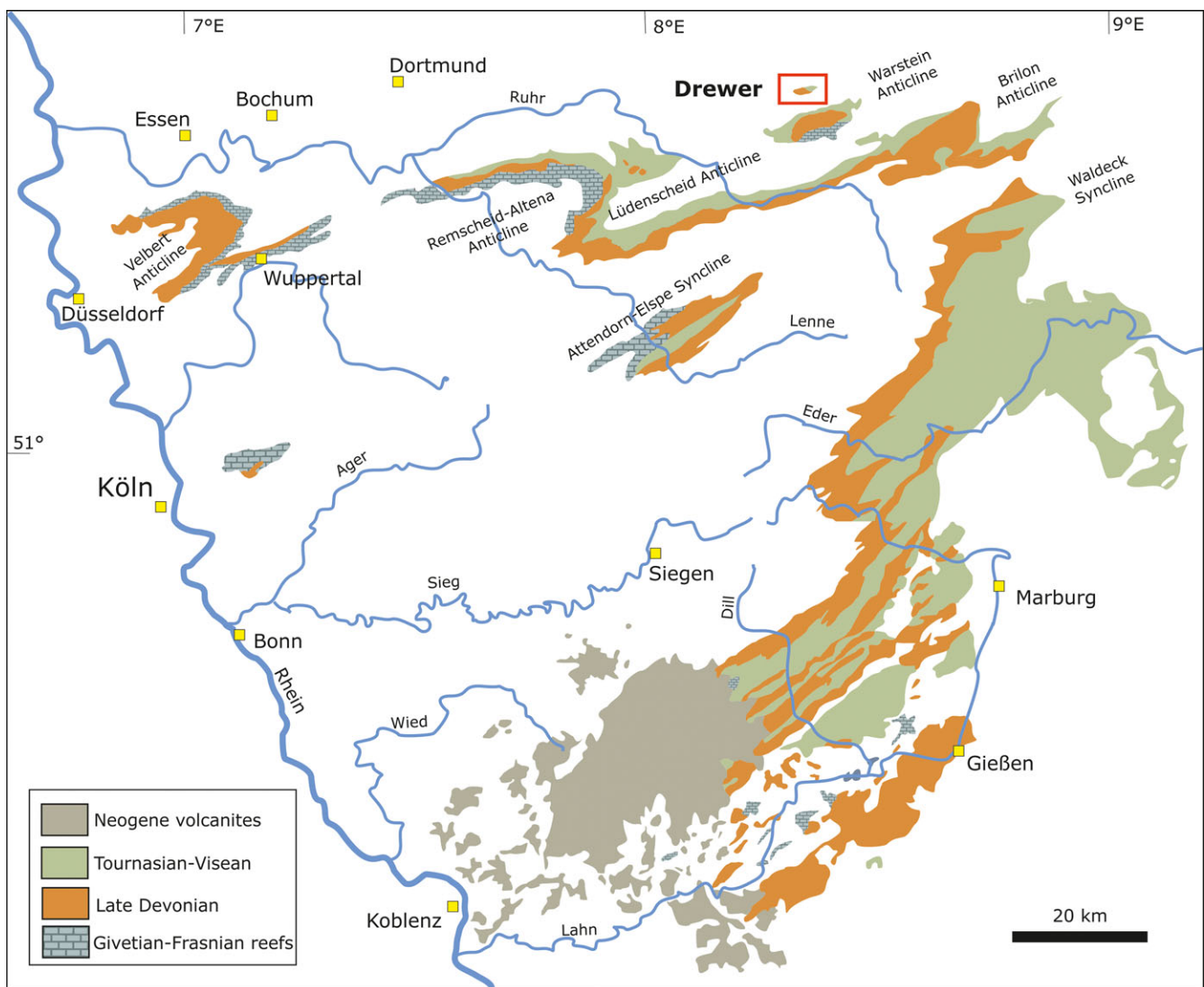
Figure 1. (Colour online) Geologic overview of the Rhenish Massif east of the Rhine river with a focus on Upper Devonian to Lower Carboniferous strata and the location of the Drewer quarry (see red box); after Königshof *et al.* (2016).

Hangenberg Event strata from India (Ganai & Rashid, 2019), Vietnam (Komatsu *et al.* 2014), China (Zhang *et al.* 2019), Morocco (Kaiser *et al.* 2007), Italy (Spalletta *et al.* 2021) and the USA (Lu *et al.* 2019; Martinez *et al.* 2019; Barnes *et al.* 2020). Facies changes are recorded at Drewer starting with the latest Famennian nodular Wocklum Limestone and the calcareous, laminated Drewer Sandstone (Luppold *et al.* 1994), followed by the Hangenberg Black Shale and intercalated Hangenberg Sandstone (Clausen *et al.* 1989). The Devonian–Carboniferous boundary at Drewer is represented by the Stockum Limestone composed of alternating limestones and marls, followed by the Lower Tournaisian Hangenberg Limestone characterized as typical cephalopod limestone (Becker *et al.* 2016). A sharp transition to phosphorus-rich black shales associated with the global Lower Alum Shale Event (cf. Becker, 1992) represents a carbonate production and ecosystem collapse during a maximum flooding event (Korn, 2010; Becker *et al.* 2016). The abrupt transition from cephalopod-rich limestones to black shales marks the lower boundary of the German Kulm facies postdating the Hangenberg Event and the Devonian–Carboniferous boundary.

The uppermost strata at Drewer features grey, crinoidal limestones, which have been correlated to the Erdbach Limestone of the southern Rhenish Massif (Becker *et al.* 2016).

3. Material and methods

The northwestern face of the Drewer quarry was logged over an 8-meter section, producing a detailed profile of the Lower Alum Black Shale facies. Thin sections of phosphorus-rich black shales were prepared. For bulk rock powder X-ray diffraction (XRD) analysis, samples were crushed to fine powder in an agate mortar. XRD analysis of carbonate-cemented background sediment was performed on a powder sample obtained with a handheld micro-drill from a polished slab. XRD measurements were carried out at the Crystallography Department (University of Bremen), using a Philips X'Pert Pro MD X-ray diffractometer with a Cu-Kα tube ($\lambda = 1.541$; 45 kV, 40 mA). Scanning electron microscopy (SEM) was conducted on a conventional tungsten filament SEM (FEI Inspect S) and a field-emission-gun scanning electron microscope with integrated focused ion beam (FEI QuantaTM 3D FEG) and an

energy-dispersive X-ray detection unit (EDAX Apollo XV) at the Institute for Geology of the University of Vienna. Data processing was conducted using the EDAX TEAM™ V3.1.1 software. The presence of pyrite was determined using a Cameca SX-100 electron microprobe at the Faculty of Geosciences, University of Bremen. Analytical conditions included an acceleration voltage of 20 kV, beam current of 10 nA and a defocussed beam of 1–2 μm diameter. Counting times were 20 seconds on peak and 10 seconds on background. For quantification natural minerals from the collections of the University of Vienna and the Smithsonian Institution were used (Jarosewich *et al.* 1980) and the built-in PAP matrix correction.

Fourier-transform infrared (FTIR) spectra were acquired from 370 to 4,000 cm^{-1} on a Bruker Tensor 27 FTIR spectrometer equipped with a glo(w)bar MIR light source, a KBr beam splitter and a DLaTGS detector at the Department of Mineralogy and Crystallography of the University of Vienna. A polished thin section was pressed on the 2 × 3 mm diamond window of a Harrick MVP 2 diamond attenuated total reflectance (ATR) accessory in such a way that either the apatite or the calcite components were predominantly probed. For comparison, spectra of blackboard chalk and a pure fluorapatite crystal from Durango, Mexico, were acquired. Sample and background spectra were averaged from 32 scans at 4 cm^{-1} spectral resolution. Background spectra were obtained from the empty ATR unit. Data handling was performed with OPUS 5.5 software (Bruker Optik GmbH, 2005).

Sample powders for carbon and oxygen stable isotope analysis of phosphate-associated carbonate (PAC) of carbonate fluorapatite were obtained from polished rock slabs using a handheld microdrill. A total of 14 samples were prepared; four from phosphatic microstromatolites, five from the phosphatic concretions and five samples from the host rock surrounding the concretions. Stable isotope analyses were conducted at IOW using a Thermo Scientific Gasbench II connected to a Thermo Finnigan MAT 253 gas mass spectrometer via a Thermo Scientific Conflo IV split interface following Böttcher *et al.* (2018). It was assumed that phosphoric acid reaction with apatite and calcite to release carbon dioxide is associated with the same kinetic $^{18}O/^{16}O$ fractionation effect (Kolodny & Kaplan, 1970; Loeffler *et al.* 2019). Isotope values given in '‰' are equivalent to 'mUr' (milli-Urey; Brand & Coplen, 2012). The carbon and oxygen isotope data are given with respect to the V-PDB standard with a reproducibility of better than ±0.10 mUr and ±0.15 mUr, respectively. Due to phase-specific sampling, the determined δ^{13}C values from the phosphatic microstromatolites represent almost pure apatite-bound inorganic carbon.

4. Results

4.a. Lithostratigraphy of the Devonian–Carboniferous boundary at Drewer

The Devonian–Carboniferous boundary section at Drewer exposes the Wocklum Limestone, Hangenberg Black Shale and Sandstone, Hangenberg Limestone, Lower Alum Black Shale, equivalents of the Erdbach Limestone and the siliceous Kulm siltstones (Fig. 2; cf. Korn *et al.* 1994; Becker *et al.* 2016). The Wocklum Limestone is grey to dark grey, nodular, partly sparitic and is well-bedded in the upper part with a sharp transition to the Hangenberg Black Shale, which is composed of darker grey to black, slaty to flaky bands of shale that are partly unconsolidated. The overlying Hangenberg Sandstone is fine grained and well sorted, with a gradational

contact to the Hangenberg Limestone above. The transitional section of the lower part of the Hangenberg Limestone comprises fine-grained siltstone with several thin nodular limestone beds, whereas the main limestone is grey and massive. The shift to the Lower Alum Black Shale is marked by thin siltstone and limestone beds, which are 10–15 cm thick (Fig. 2). The Lower Alum Black Shale measures approximately 130 cm in thickness and is described in detail below. The grey to dark grey, massive, mostly sparitic Erdbach Limestone above the Lower Alum Black Shale is approximately 80 cm thick, followed by the black, very fine-grained, siliceous Kulm siltstone.

4.b. Lithostratigraphy of the Lower Alum Black Shale interval at Drewer

The detailed profile of the Lower Alum Black Shale (Fig. 3) begins with the uppermost parts of the Hangenberg Limestone, a micritic, bioclastic wackestone (cf. Becker *et al.* 2016) that grades into weakly carbonaceous siltstones representing the last phase of deposition before the Lower Alum Shale Event. The Lower Alum Black Shale interval at Drewer has been divided into nine units, which are designated as units 5a to 5i (Fig. 3). Unit 5a comprises 40 cm of dark grey clay with pyrite-bearing intervals and 0.5–10 mm thick beds. Unit 5b includes 30 cm of a similar lithology as unit 5a with clay, as well as first occurrences of isolated, tabular phosphatic concretions up to 2 cm in width and 0.5 cm in thickness. Unit 5c is similar in appearance with more individual tabular concretions, which occur more frequently in unit 5d. In this unit, various concretion morphologies from tabular to platy to nodular are present (Fig. 3). Unit 5e shows wavy lamination within the finely bedded shales, as well as cracks and fissures filled with weathered material. Unit 5f exhibits a clear transition from unit 5e marked by numerous horizontal, tabular and partly overlapping phosphorite beds (Figs. 3, 4a). This bed is characterized by its greyish colour and more abundant concretions (Fig. 3). Units 5g and 5h are replete in nodular to oval concretions measuring up to 10 cm in width that occur in close proximity to each other (Fig. 3). Unit 5i is the uppermost Lower Alum Black Shale unit at Drewer and features wavy lamination and tabular, elongated and occasionally irregular and fragmented concretions orientated with their long axes parallel to bedding (Figs. 3, 4). Some smaller concretions are spherical. This unit is capped by a sharp transition to the pyrite-bearing, dark grey, Erdbach limestone (Fig. 3).

4.c. Petrography, mineralogy and stable isotope geochemistry

Lower Alum Black Shale unit 5h was chosen for sampling and detailed investigation due to its high content of phosphatic concretions (Fig. 5). Two microfacies were identified in these samples referred to as microfacies 1 and 2 from hereon (cf. Fig. 5a). Microfacies 1 is composed of silty shales and mudrocks featuring a pelitic matrix with poorly sorted components that comprises around 10% of the total volume. The components are mostly angular, detrital quartz grains with subordinate occurrences of muscovite and minor pyrite. X-ray diffraction patterns further revealed the presence of minor dolomite and ferroan dolomite. Microfacies 2 contains poorly sorted, angular quartz grains with subordinate dolomite and muscovite, as well as phosphatic minerals and large phosphatic concretions (Fig. 5). Microfacies 2 contains radiolarians and subordinate conodonts, and the portion of rock fragments and quartz components is estimated at
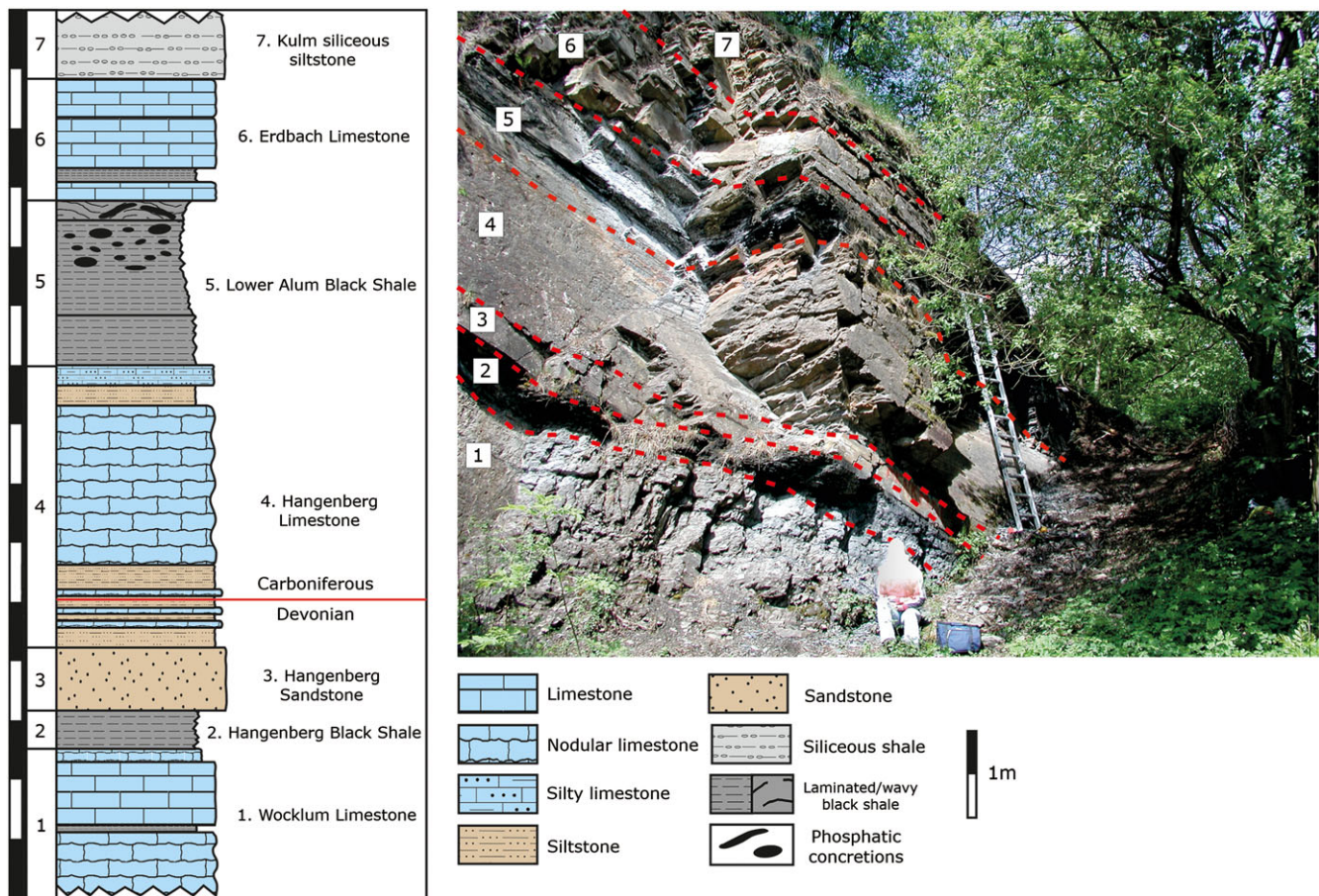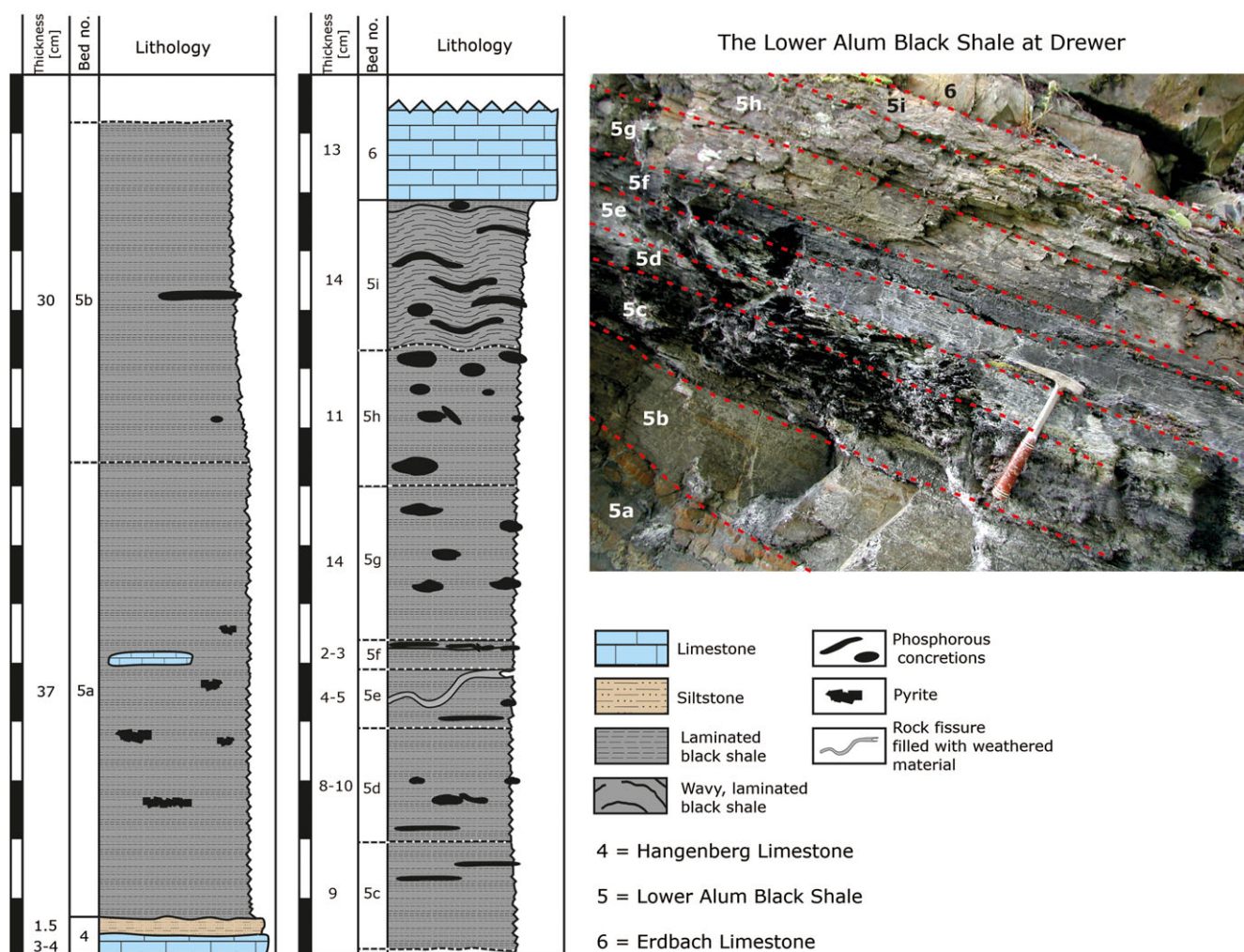
Figure 2. (Colour online) Outcrop photograph and sedimentary log of the investigated outcrop in the Drewer quarry; person for scale.

20–30 vol.%. The phosphatic concretions occur as spherical, oval and elongated forms that are between 1 and 4 cm in size. The phosphatic concretions can be distinguished in two different types. The first type of these concretions is oval to spherical and exhibits well-defined contours at their margins. These concretions contain a matrix of cryptocrystalline carbonate fluorapatite, as well as poorly preserved radiolarians that occupy an estimated 5% of the concretion volume. The second type of concretions grew around the first type of concretions exhibiting less well-defined contours at their margins (Fig. 5) and may reach up to 8 cm in diameter. The texture, fabric and mineral content of these concretions are similar to that of microfacies 2, but they contain more carbonate fluorapatite compared to quartz.

Phosphatic microstromatolites occur in two morphologies. The first type are aggregates of thin columns showing well-defined lamination (Fig. 6a, b), which measure up to 250 µm in diameter and reach 600 µm in length. Some columns are shorter and show a cauliflower-like morphology (Fig. 6b). Some of the microstromatolites of this type occur within the outer parts of phosphatic concretions (cf. Fig. 5d), where much of the space between individual columns is occupied by microcrystalline silica (Fig. 6a, b). The second type of microstromatolite corresponds to smaller aggregates within the outer concretions (Fig. 6c, d). This type of microstromatolite does not exhibit any columnar or branching morphologies, yet it shows well-defined lamination within bulbous aggregates. Both types of microstromatolites contain unevenly

distributed, authigenic pyrite (Figs. 6, 7). Most common are columnar and branching microstromatolites attached to the outer rim of the inner concretion (cf. Fig. 7a, c, d), with some concretions completely encased by microstromatolites (Fig. 7a–d). The individual stromatolite columns show a fine lamination (Fig. 7e, f).

Scanning electron microscopy confirms that the microstromatolites within the phosphatic concretions are composed predominantly of apatite revealing a light grey appearance distinct from purely siliciclastic components in backscatter imaging (Fig. 8). The alternating fine laminae within the microstromatolites contain different amounts of alumosilicates and microcrystalline silica. The columnar stromatolites attached to the inner concretion show varying degrees of siliciclastics (Fig. 8a, b) and engulf radiolarian tests that consist of silica (Figs. 8c, 9c). Discernible laminae are composed mainly of alumosilicates, whereas the bulk of the stromatolites is composed of phosphorus minerals (Fig. 9b–d). Pyrite aggregates are prominent in backscatter mode by their strong white reflection (Fig. 8c, d). Electron microprobe analyses revealed that authigenic pyrite occurs within the second-generation concretions and within phosphatic microstromatolites (Fig. 8c, d), yet no pyrite was detected in the first-generation concretions. Pyrite within the second-generation concretions shows iron and sulphur contents between 40.3 and 47.1 wt% and 44.5 and 54.1 wt%, respectively (compared to 47.0 and 47.4 wt% iron and 53.8 and 54.3 wt% sulphur in the standard material), with average contents of 44.7 wt% iron and 51.4 wt% sulphur. Pyrite contains

Figure 3. (Colour online) Detailed lithostratigraphic log and an outcrop photograph showing the corresponding beds of the Lower Alum Black Shale at Drewer; hammer for scale.

accessory elements including arsenic (averaging 0.19 wt%), cobalt (averaging 0.19 wt%), nickel (averaging 0.63 wt%), copper (averaging 0.12 wt%) and zinc (averaging 0.03 wt%). Pyrite analysed within the phosphatic microstromatolites shows average iron and sulphur contents of 44.9 and 52.8 wt%, respectively. This pyrite contains accessory elements including arsenic (averaging 0.08 wt%), cobalt (averaging 0.09 wt%), nickel (averaging 0.9 wt%), copper (averaging 0.07 wt%) and zinc (averaging 0.01 wt%).

FTIR ATR spectra of the mineral composition of the outer concretion, inner concretion and the phosphatic microstromatolites (cf. Fig. 5d) were compared to spectra of pure carbonate-free fluorapatite from Durango, Mexico (Becker *et al.* 2016), a carbonate fluorapatite from Limburg an der Lahn, Germany (RRUFF data base R050529; ca. 20% of the phosphate sites is substituted by carbonate; Downs, 2006; Lafuente *et al.* 2015) and a calcite reference acquired from a piece of blackboard chalk (Fig. 10). The wavenumber region from 400 to 1,600 cm^{-1} was chosen because it displays all fundamental vibrations of the phosphate and carbonate anion groups (White, 1974; Böttcher *et al.* 1997; Penel *et al.* 1997). Regarding the exact peak positions, it must be emphasized that strong vibrational bands in ATR spectra are slightly red-shifted to lower wavenumbers due to the impact of

the complex refractive index instead of pure absorption (Harrick, 1967). Whereas pure, carbonate-free fluorapatite shows only the overlapping stretching bands ν_1 and ν_3 (ca. 1,100 to 930 cm^{-1}) and bending modes ν_2 and ν_4 (ca. 630 to 540, 470 cm^{-1}) of the phosphate groups, with a flat baseline above 1,100 cm^{-1}, the outer and inner concretion and the microstromatolites, as well as the carbonate fluorapatite from the RRUFF database shows additional characteristic bands at approximately 1,425 and 1,450 cm^{-1} (double-headed arrows in Fig. 10); the latter bands have been assigned to the anti-symmetric stretching vibrations ν_3 of the carbonate group replacing phosphate (substitution type B) in the apatite structure (Hofmann, 1997). The spectra of these three Drewer apatites also reveal minor vibrational bands (ν_2, ν_3, ν_4) caused by the carbonate group, positioned at about 1,400, 860 and 710 cm^{-1}, respectively (cf. White, 1974; Böttcher *et al.* 1997). These results confirm the presence of carbonate groups in the structure of apatite from the Drewer concretions and microstromatolites.

The carbon stable isotope compositions of carbonate fluorapatite show some differences between the phosphatic microstromatolites, the phosphatic concretions and the host rock. $\delta^{13}C$ values of phosphatic microstromatolites are lowest ranging between −3.3 and −2.2‰, whereas those of phosphatic concretions are less negative between −1.7 and −0.8‰ (Fig. 11).
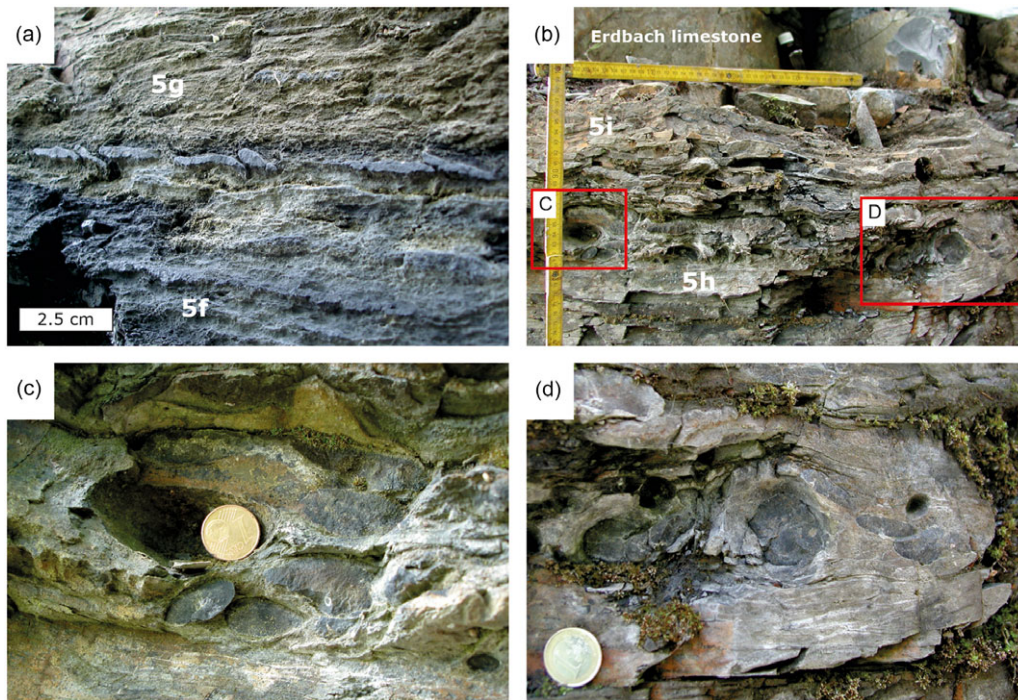
Figure 4. (Colour online) Outcrop photographs of the Lower Alum Black Shale at Drewer. (a) Elongated, flat phosphatic concretions within the transition of beds 5f to 5g. (b) Bed 5h with larger, oval to spherical phosphatic concretions overlain by bed 5i and the Erdbach limestone; folding rule for scale. (c) Detail corresponding to the left red rectangle in (b) showing numerous oval phosphatic concretions within bed 5h; coin for scale. (d) Detail corresponding to the right red rectangle in (b) with spherical phosphatic concretions within laminated black shales from bed 5h; coin for scale.
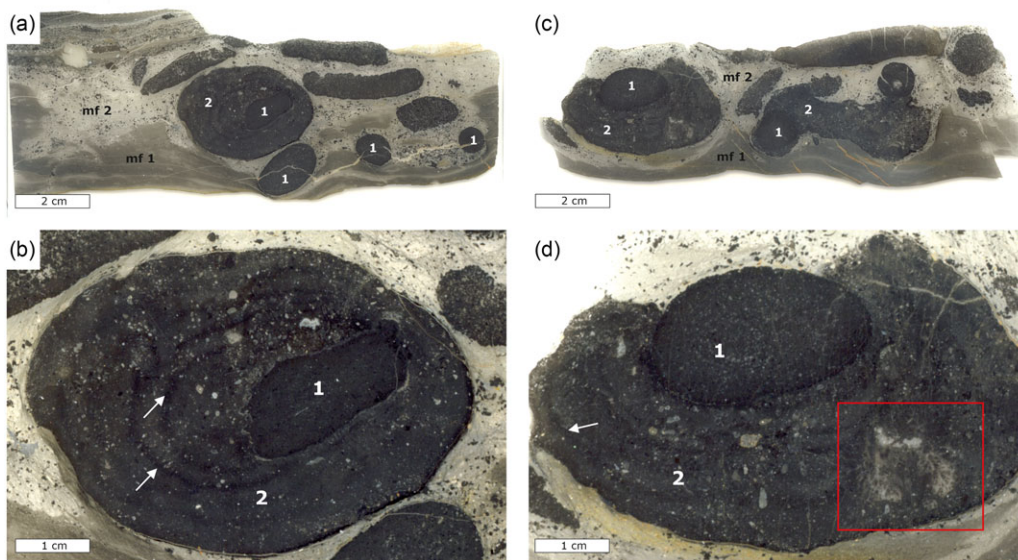
Figure 5. (Colour online) Thin section scans and photomicrographs of phosphatic concretions from bed 5g of the Lower Alum Black Shale; mf = microfacies, 1 = first-generation concretion, 2 = second-generation concretion. (a) Thin section scan showing two microfacies of background sediment with numerous smaller spherical, oval and elongated concretions and a large concretion floating within microfacies 2. (b) Close-up view of the larger phosphorous concretion in (a) with the first- and second-generation concretions, whereby the latter completely surrounds the former. White arrows show growth rims in the second-generation concretion. (c) Thin section scan showing microfacies 1 and 2 with numerous smaller concretions and a large concretion floating within microfacies 2. (d) Detailed view of the large concretion in (c) showing the second-generation concretion not completely surrounding the first-generation concretion. Arrows denoting a vague laminated growth pattern in the outer concretion, and the red rectangle highlighting a large aggregate of columnar branching phosphatic microstromatolites within the second-generation concretion.

The $\delta^{13}C$ values of the host rock are between -1.7 and -1.3‰. $\delta^{18}O$ values follow a similar trend; the microstromatolites show the most negative values between -9.1 and -7.9‰, whereas those of the concretions and the host rock lie between -8.1 and -7.3‰. The $\delta^{18}O$ values of the host rock fall into a narrower range between -7.8 and -7.5‰.
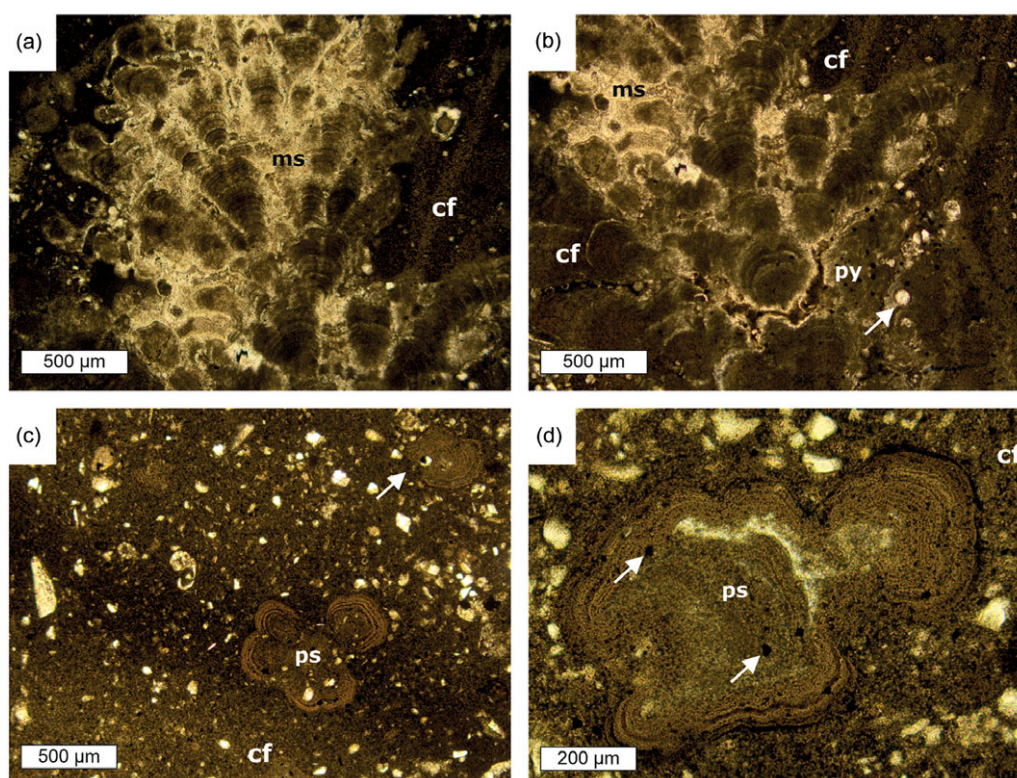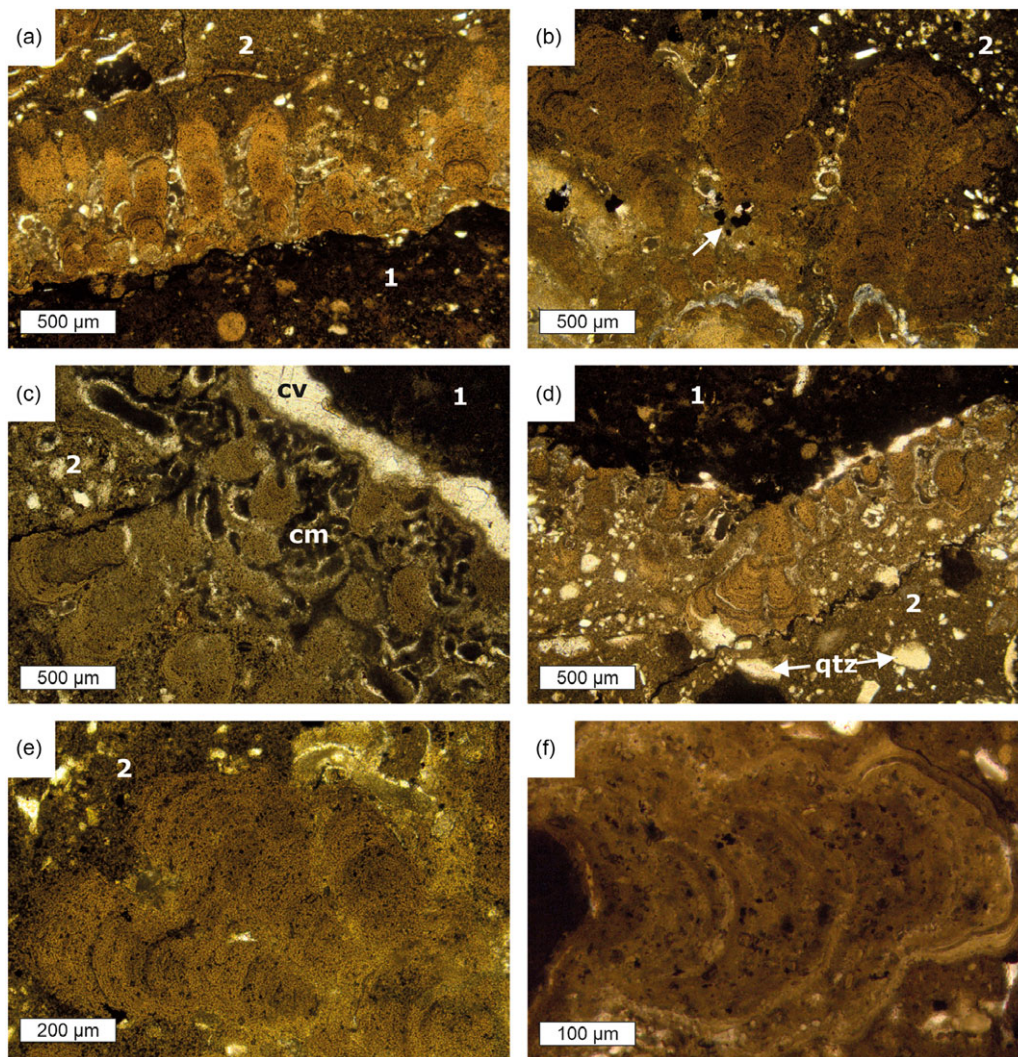
Figure 6. (Colour online) Photomicrographs of phosphatic microstromatolites; ps = phosphatic microstromatolite, ms = microcrystalline silica, cf = carbonate fluorapatite, py = pyrite. (a, b) Large aggregates of columnar branching microstromatolites floating within the second concretion with abundant microcrystalline silica between individual columns. (b) An aggregate of more bulbous, cauliflower-shaped microstromatolites with microcrystalline silica and pyrite (opaque minerals); arrow denoting a radiolarian test. (c) Small aggregates of microstromatolites floating within the phosphatic second-generation concretion, arrow denoting a smaller aggregate. (d) Close-up view of a microstromatolite aggregate exhibiting small-scale darker and lighter laminae; arrows denoting authigenic pyrite within the phosphatic microstromatolite.

5. Discussion

5.a. Phosphogenesis and concretion growth

The Lower Alum Black Shale represents a period of reduced carbonate and clastic sedimentation, as well as high degrees of eutrophication and marine organic productivity leading to anoxic conditions in the sediments and possibly in the bottom waters (Siegmund *et al.* 2002; Rakocinski *et al.* 2023). These conditions are similar to present-day upwelling zones, where the lack of oxygen in sediments and bottom waters facilitates the accumulation of phosphorus released during organic matter remineralization (Lomnitz *et al.* 2016). The Lower Alum Shale Event has been interpreted as a global anoxic event leading to a severe regional extinction of many invertebrate groups (Becker, 1992; Walliser, 1996; Kaiser *et al.* 2011) culminating in a sea-level highstand during the Mississippian (Kaiser *et al.* 2011; Becker *et al.* 2021). The Lower Alum Shale Event is also represented by black shales and cherts in the Holy Cross Mountains in Poland and from the Lydiennes Formation in the Montagne Noire, southern France. These black shale deposits provide evidence for dysoxic to anoxic conditions in bottom waters, as well as photic zone euxinia (Rakocinski *et al.* 2021, 2023), probably favoured by enhanced productivity in surface waters. Since the same environmental constraints are probably applicable to the area of the Drewer locality, it suggests that the prolonged sea-level highstand with eutrophication in the photic zone (cf. Siegmund *et al.* 2002) favoured phosphogenesis at Drewer. The scarcity or the lack of bioturbation in the black shales at Drewer (Siegmund *et al.* 2002; own observation) agrees with episodically anoxic bottom water conditions.

Phosphogenesis in black shales and other organic-rich deposits is commonly manifested in the form of laminated crusts, lithified hardgrounds and gravels, disseminated nodules and oval to spherical concretions (Glenn *et al.* 1994; Scasso & Castro, 1999; Arning *et al.* 2009a, Bradbury *et al.* 2015; Filek *et al.* 2021). Today, authigenic phosphate crusts, nodules and concretions precipitate in organic-rich sediments at shallow depth (Soudry, 2000; Arning *et al.* 2009a), deposited either below upwelling or oxygen minimum zones (Föllmi, 1996; Arning *et al.* 2008). The depletion of oxygen is a critical factor because it favours the preservation of organic matter, which is required as a phosphorus source during phosphogenesis (Filippelli, 2011). The Lower Alum Black Shale at Drewer exhibits two concretion types, which are interpreted as representing two different generations of growth (Fig. 5). The first generation is represented by spherical to oval phosphate aggregates, which are overgrown by a second generation that accreted a larger volume of phosphorite (Fig. 5c, d). The first generation of phosphatic concretions grew in organic-rich sediments corresponding to microfacies 1 and were possibly exposed by winnowing. After their exposure, the phosphatic concretions were apparently transported from their formation site into sediments corresponding to microfacies 2. The composition of first-generation concretions differs from microfacies 2, which also suggests that they did not grow in microfacies 2 sediments but were redeposited before the second generation of concretions formed. Different formation conditions for the two generations of concretions are further indicated by the absence of authigenic pyrite within the first-generation concretions, while pyrite is abundant within the second-generation concretions and in the

Figure 7. (Colour online) Photomicrographs of columnar branched phosphatic microstromatolites attached to the first-generation concretion; 1 = first-generation concretion, 2 = second-generation concretion, cv = carbonate vein, cm = clay minerals, qtz = quartz grains. (a) Columnar microstromatolites attached to the first-generation concretion. (b) Columnar, branched microstromatolites attached to the first-generation concretion, arrow denoting pyrite aggregates. (c, d) Columnar microstromatolites among clay minerals from a carbonate vein on the surface of the first-generation concretion. (e, f) Close-up view of columnar microstromatolites showing fine alterations of darker and lighter laminae among dispersed clay minerals and pyrite.

microstromatolites. In contrast to the first-generation concretions, second-generation concretions incorporated more non-phosphate minerals including clay minerals during growth (Figs. 5, 8, 9). These non-phosphate minerals were most likely incorporated from microfacies 2, suggesting that the second-generation concretions grew *in situ* within this microfacies. In addition, the second-generation concretions exhibit several growth rims that suggest multiple phases of concretion growth within microfacies 2 sediments (Fig. 5b, d). The presence of pyrite dispersed within the second-generation concretion (Fig. 8d) suggests that conditions remained sulphidic within the sediment during the growth of the phosphatic concretions within the Lower Alum Black Shale at Drewer.

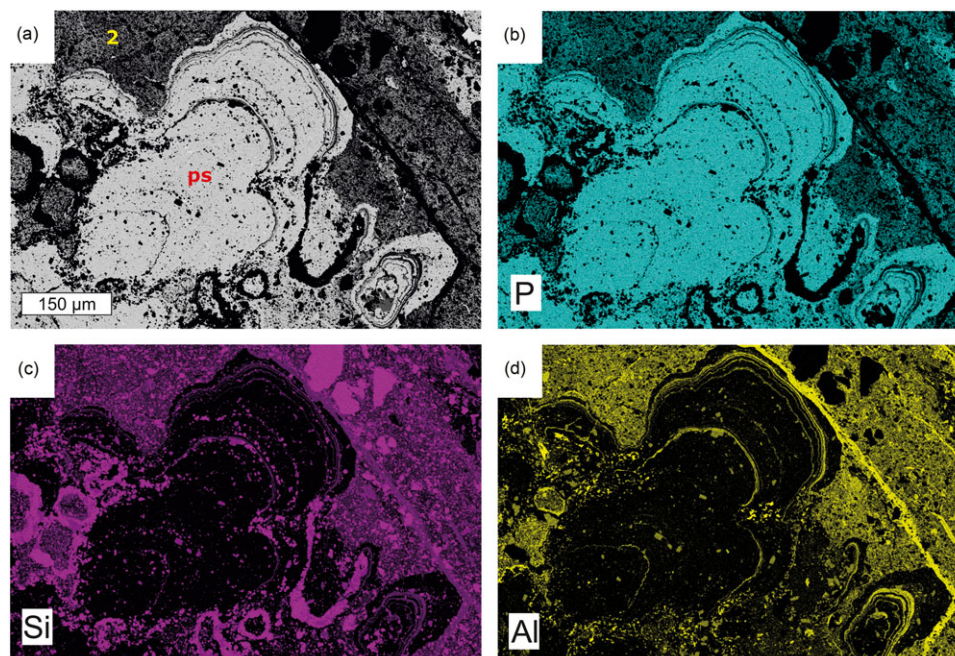## 5.b. Phosphatic microstromatolites – Palaeoenvironment and palaeoecology

Three possible mechanisms for microbial phosphorus accumulation include the remineralization of organic matter by sulphate-reducing bacteria, the release of internally stored (poly)phosphate by giant chemotrophic sulphide-oxidizing bacteria and the reductive dissolution of iron oxides that release adsorbed phosphorus (Froelich, 1988; Schulz & Schulz, 2005; Arning *et al.* 2009a; Berndmeyer *et al.* 2012). Microbial sulphate reduction is the

quantitatively dominant anaerobic process in the remineralization of organic matter in modern continental margin sediments (Ferdelman *et al.* 1999; Brüchert *et al.* 2003). Sulphate reduction is considered as a main cause of liberating phosphorus from organic matter, enabling the formation of phosphorite crusts and nodules in modern upwelling sediments (Arning *et al.* 2009a, 2009b). The Lower Alum Black Shale would have provided much organic matter for sulphate-reducing bacteria to release dissolved phosphorus to sedimentary pore water. The distribution, abundance and morphology of authigenic pyrite are further indicators for sulphate reduction in ancient phosphate-rich deposits (Wilkin *et al.* 1996; Cosmidis *et al.* 2013; Rickard, 2021). Pyrite is abundant within the second-generation phosphatic concretions and within the microstromatolites (Figs. 8a, c, d, 9f). The remineralization of organic matter and phosphorus release by sulphate reduction probably contributed substantially to phosphogenesis in the organic-rich sediments at Drewer, suggesting that phosphogenesis during early diagenesis was the primary process during growth of the second-generation concretions and microstromatolites.

Phosphorus-rich deposits in modern upwelling regions provide habitats for giant chemotrophic sulphide-oxidizing bacteria (Schulz & Schulz, 2005; Arning *et al.* 2008; Crosby & Bailey, 2012). The release of phosphate from internally stored (poly) phosphate compounds to pore waters has been demonstrated for
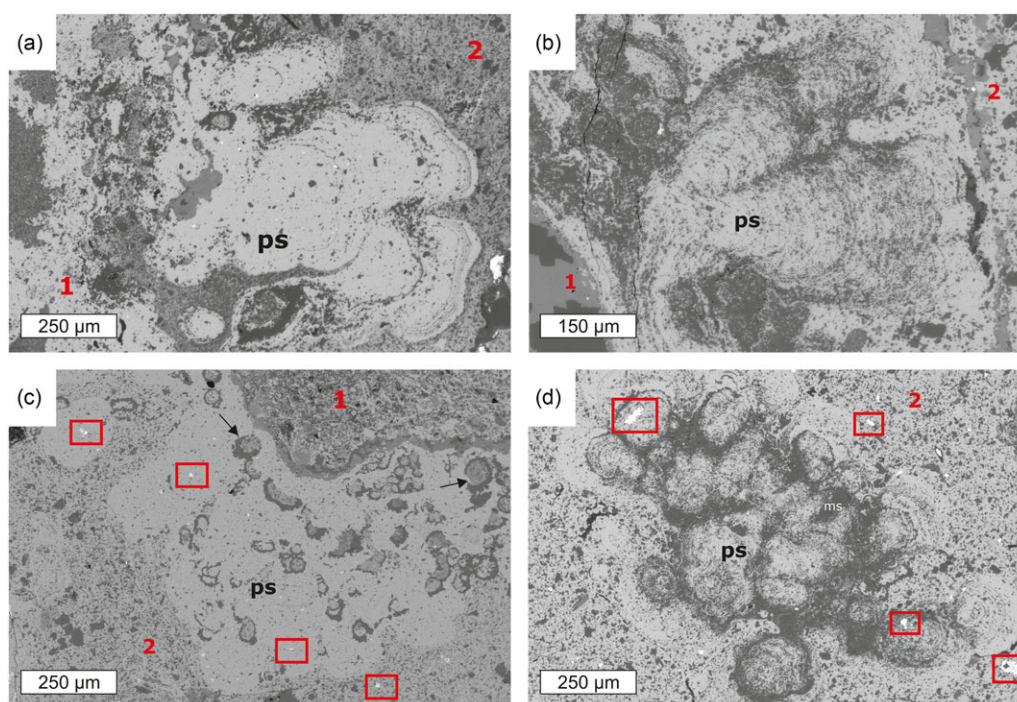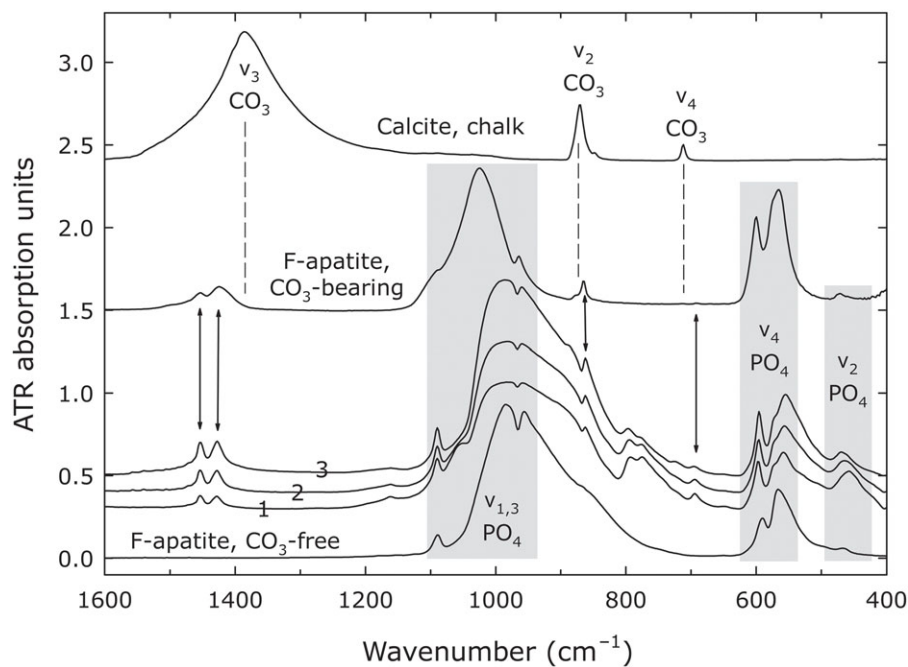
Figure 8. (Colour online) Scanning electron microscopy images of phosphatic microstromatolites; 1 = first-generation concretion, 2 = second-generation concretion, ps = phosphatic microstromatolite, ms = microcrystalline silica. (a) Bulbous microstromatolite projecting from the first-generation concretion outwards and showing thin dark laminae of mostly alumosilicates, as well as finely dispersed pyrite (white reflecting minerals). (b) Columnar microstromatolite attached to the first-generation concretion with more intense, frequent interlayering of alumosilicates. (c) Bulbous to cauliflower-shaped microstromatolite with little lamination; red rectangles denoting authigenic pyrite, arrows denoting radiolarian tests. (d) Apparently free-floating microstromatolite aggregate within the second-generation concretion among abundant microcrystalline silica; red rectangles highlighting larger pyrite aggregates within the microstromatolite and the second-generation concretion.

Figure 9. (Colour online) Scanning electron microscope element mapping; ps = phosphatic microstromatolite, 2 = second-generation concretion, P = phosphorus, Si = silicon, Al = aluminium. (a) Electron backscatter image of a phosphatic microstromatolite. (c–d) Element distribution map of a phosphatic microstromatolite attached to the first-generation concretion.

the genera *Beggiatoa* and *Thiomargarita*, which can act as microbial drivers of phosphogenesis in organic-rich sediments (Schulz & Schulz, 2005; Goldhammer *et al.* 2010). Studies on ancient phosphate-rich deposits suggest that sulphide-oxidizing bacteria similar to present-day *Thiomargarita* and *Beggiatoa* existed since the Proterozoic (Bailey *et al.* 2007; Lepland *et al.* 2013;

Figure 10. Fourier-transform infrared (FTIR) attenuated total reflectance (ATR) spectra. Spectra of (1) first-generation concretion, (2) second-generation concretion, and (3) phosphatic microstromatolite, as well as blackboard chalk, carbonate-bearing fluorapatite (RRUFF database; Downs, 2006; Lafuente et al. 2015), carbonate-free fluorapatite from Durango, Mexico (Becker et al. 2016); broken lines and shaded areas indicate the positions and areas of certain vibrations of the anion groups. The two double arrows at ca 1,425 and 1,450 cm^{-1} indicate the anti-symmetric stretching ν_3 modes of B-type carbonate groups in apatite. Spectra have been vertically normalized and offset for better visibility. See text for details.
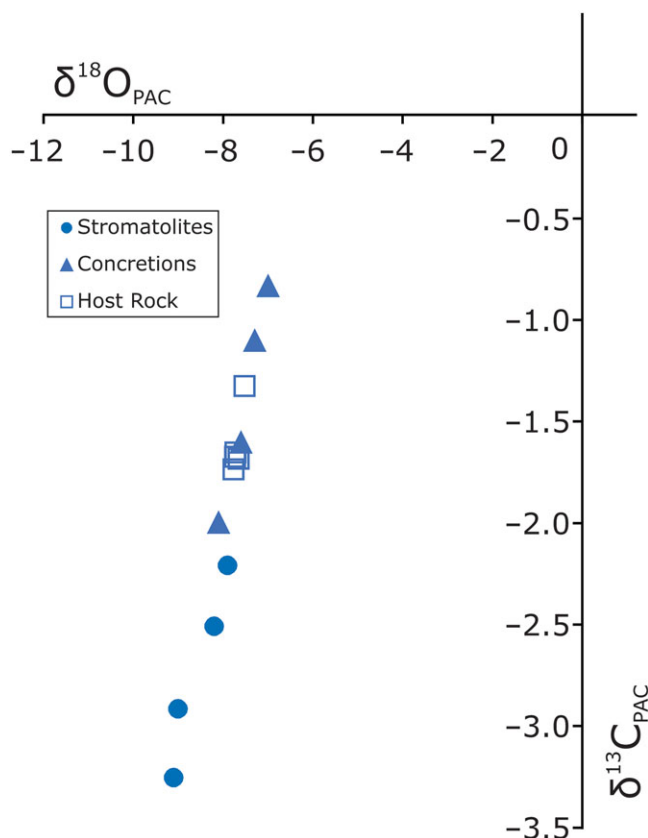
Figure 11. (Colour online) Cross plot showing carbon and oxygen stable isotope compositions of phosphate-associated carbonate (PAC) of the phosphatic microstromatolites, phosphatic concretions and the phosphatic microfacies 2 of the host rock.

Czaja et al. 2016); these chemotrophic bacteria are known to dwell in specific horizons at the redox boundary or in narrow zones at the sediment–water interface, contributing to the formation of phosphorite laminites and crusts on the seafloor (Jørgensen & Revsbach, 1983; Arning et al. 2008, 2009a). Although evidence of the involvement of sulphide-oxidizing bacteria in phosphogenesis at Drewer is lacking, their possible contribution cannot be excluded.

An alternative microbial consortium that could have formed the phosphatic microstromatolites are microorganisms forming *Frutexites*, which are laminated, arborescent ferruginous or manganiferous microstromatolites that form in low-energy environments typified by low sedimentation rates and limited oxygen availability (Reitner et al. 1995; Woods & Baud, 2008; Lazar et al. 2013). Although it is not entirely clear which microbial consortia are involved in the formation of ancient *Frutexites*, iron enrichment appears to be a primary feature leading to the interpretation that iron-oxidizing bacteria in conjunction with either nitrate or sulphate reduction are key players in their development (Jakubowicz et al. 2014; Heim et al. 2017). Many *Frutexites* have been interpreted as stromatolites dwelling in deep-water or cryptic habitats that show no preferred phototactic growth direction (Böhm & Brachert, 1993; Gischler et al. 2021). Although the morphology and size of the Drewer microstromatolites are similar to reported *Frutexites*, the lack of iron oxides in the samples and the formation environment of the concretions argues against this interpretation (cf. Crosby et al. 2014). If bottom and pore waters were indeed anoxic to sulphidic at Drewer as suggested by trace element analyses (Siegmund et al. 2002; Becker et al. 2016) and by the presence of pyrite, an accumulative mechanism by the formation and subsequent dissolution of iron oxides would be difficult to achieve and attain, although this may depend on the intensity and expansion of reducing bottom water conditions (Dellwig et al. 2010).

5.c. Stable isotopes and a scenario of microstromatolite and concretion formation

The $\delta^{13}C_{PAC}$ values of the phosphatic microstromatolites between −3.5 and −2‰ (Fig. 11) probably do not record early- to mid-

Tournaisian seawater dissolved inorganic carbon (DIC). Carbon isotope stratigraphy from the Devonian–Carboniferous boundary suggests high rates of organic carbon burial and drawdown of atmospheric carbon dioxide as evidenced by positive $\delta^{13}C$ excursions across this interval from localities in Europe, China and the USA (Buggisch & Joachimski, 2006; Myrow *et al.* 2011; Kumpan *et al.* 2014; Kaiser *et al.* 2015; Qie *et al.* 2015). These excursions show a variety of $\delta^{13}C$ peaks between +2 and +6‰ and are difficult to correlate globally as they differ between various regions and basins, which makes a reliable reconstruction of the carbon isotope composition of global ocean DIC difficult (Kaiser *et al.* 2015; Paschall *et al.* 2019; Barnes *et al.* 2020). A lack of positive $\delta^{13}C$ excursions during the Middle and Late Devonian of the Drewer section was noted by Buggisch & Joachimski (2006), who attributed this lack to a stratigraphic gap where no carbonates were deposited. Kumpan *et al.* (2015) investigated the $\delta^{13}C$ record at Drewer, yet concluded that diagenetic alteration had compromised any reliable $\delta^{13}C$ record of seawater. However, a positive $\delta^{13}C$ excursion was documented in the Hasselbachgraben section near Oberrödinghausen, which is in the vicinity of the Drewer locality (Kaiser *et al.* 2006). These $\delta^{13}C$ excursions were assigned to the Hangenberg Shale Event and interpreted as a sea-level highstand at the peak of the Hangenberg crisis (Kaiser *et al.* 2006). Although chemostratigraphic data directly related to the Lower Alum Shale Event are sparse (e.g. Saltzman *et al.* 2004), Buggisch *et al.* (2008) reported a positive carbon isotope excursion during this event from coeval sections across Europe, reporting $\delta^{13}C_{carbonate}$ values as high as +5‰.

The $\delta^{13}C$ composition of seawater DIC during the Late Devonian Hangenberg Shale Event until and after the Lower Alum Shale Event was strongly influenced by positive $\delta^{13}C$ excursions reflecting perturbations in the global carbon cycle. Moreover, carbonate $\delta^{13}C$ values from the latest Devonian through to the mid-Tournaisian never dropped below 0‰, which is distinct from $\delta^{13}C$ values determined for the phosphatic stromatolites and concretions at Drewer (cf. Fig. 11). The $\delta^{13}C$ values of the Drewer phosphatic microstromatolites are more negative compared to the $\delta^{13}C$ value of Early Carboniferous seawater DIC (Saltzman *et al.* 2004; Buggisch *et al.* 2008). Moreover, the $\delta^{13}C$ values of phosphatic microstromatolites are also more negative than $\delta^{13}C$ values of the phosphatic concretions and the host material of microfacies 2 (Fig. 11). Inorganic carbon incorporated by phosphate minerals during phosphogenesis was likely a mixture of seawater DIC and DIC that was formed during the anaerobic microbial remineralization of organic matter in the sediment.

The lower $\delta^{13}C$ values of the Drewer microstromatolites compared to phosphatic concretions and host rock suggest that the metabolism of the mat-forming microorganisms may have been responsible for local fractionation of stable carbon isotopes within the microbial mats that formed the microstromatolites. All $\delta^{13}C$ values are substantially lower than what would be expected by fractionation during Calvin cycle carbon fixation mediated by oxygenic phototrophic microbial communities (O'Leary, 1988; Laws *et al.* 1995). Although a covariance of $\delta^{13}C$ and $\delta^{18}O$ values of microstromatolites ($r^2 = 0.94$) and the phosphatic concretions ($r^2 = 0.97$) may argue for some degree of diagenetic overprint with meteoric waters during burial diagenesis (cf. Brand & Veizer, 1981; Banner & Hanson, 1990; Heydari *et al.* 2001; Tong *et al.* 2016), the $\delta^{13}C$ values of the microstromatolites are still more negative than those determined for the phosphorous concretions and the host rock, suggesting that the signal of microbial fractionation has been preserved to some degree. Moreover, environmental perturbations

related to climatic warming may cause shifts of $\delta^{13}C$ and $\delta^{18}O$ to more negative values as observed for the Paleocene – Eocene Thermal Maximum and several oceanic anoxic events (Zachos *et al.* 2006; Ullmann *et al.* 2014). Therefore, the observed covariance between $\delta^{13}C$ and $\delta^{18}O$ values of the phosphatic concretions and microstromatolites may additionally be impacted by climatic warming, elevated organic matter burial and increasing seawater temperatures from the late Famennian to the early Tournaisian (cf. Kaiser *et al.* 2008). Based on the temperature dependence of oxygen isotope fractionation between carbonate minerals, carbonate-bearing apatite and water (O'Neil *et al.* 1969; Loeffler *et al.* 2019) and neglecting site-specific isotope fractionation (Zheng, 2016; Aufort *et al.* 2017), the observed maximum isotope variation (Fig. 11) would indicate a temperature rise by up to 8 and 11°C. This seems to be unrealistically high, therefore, at least parts of the oxygen isotope shift may be caused by a lowering in the oxygen isotope composition and therefore salinity of the pore water. Taken together, it is likely that the $\delta^{13}C$ values of the phosphatic microstromatolites do not reflect ambient seawater composition, suggesting that the incorporated carbon within the carbonate fluorapatite reflects microbial fractionation related to a non-phototrophic metabolism.

The phosphatic concretions formed in anoxic sediments with the oxic–anoxic interface likely present in the water column in a regime of low water energy and low sedimentation rates. Some first-generation concretions are completely surrounded by the phosphatic microstromatolites (Figs. 5c, d, 6a, c, d), with the concretions as a substrate for the growth of stromatolite-forming microbial mats. The growth direction of the microbial mats was highly variable, showing no unidirectional upward growth direction as would be expected for phototactic growth as observed for photosynthesis-based cyanobacterial stromatolites (Allwood *et al.* 2006, 2007). Interestingly, chemotrophic microbial mats growing around carbonate concretions have also been observed at methane seeps in the Black Sea (Reitner *et al.* 2005). There, the mat-forming methanotrophic archaea and sulphate-reducing bacteria form thin layers around the concretions, showing a growth mode similar to the Drewer microstromatolites. It cannot be ruled out that some of the microstromatolites formed during reworking of the concretions at the sediment water interface, yet it is unlikely that the delicate branching stromatolites (Fig. 7) would have been preserved during physical reworking, sedimentation and burial of the concretions. The envisaged scenario of microstromatolite formation on phosphatic concretions is depicted schematically in Fig. 12. The first-generation concretions formed within deep-water anoxic, organic carbon-rich sediments during the global sea-level highstand of the Lower Alum Shale Event. The high content of organic matter and anoxic conditions allowed for the accumulation of phosphorus and the formation of phosphatic concretions (Fig. 12a). These first-generation concretions were subsequently moved from their original locus of formation, either by winnowing, bottom currents, or mass wasting and transported into a host sediment consisting of microfacies 2 sediments (Figs. 5, 12b). The phosphatic concretions were then colonized within the soft and porous sediment by microbial mats, probably including sulphate-reducing bacteria. These bacterial mats used the first-generation concretions as templates for biofilm attachment, growing on all sides of the concretions by displacive growth, pushing the soft surrounding sediments outwards, away from the concretion (Fig. 12c). The stromatolite-forming microbial mats showed no preferred growth direction that would suggest phototactic growth, which is in line with the interpretation that
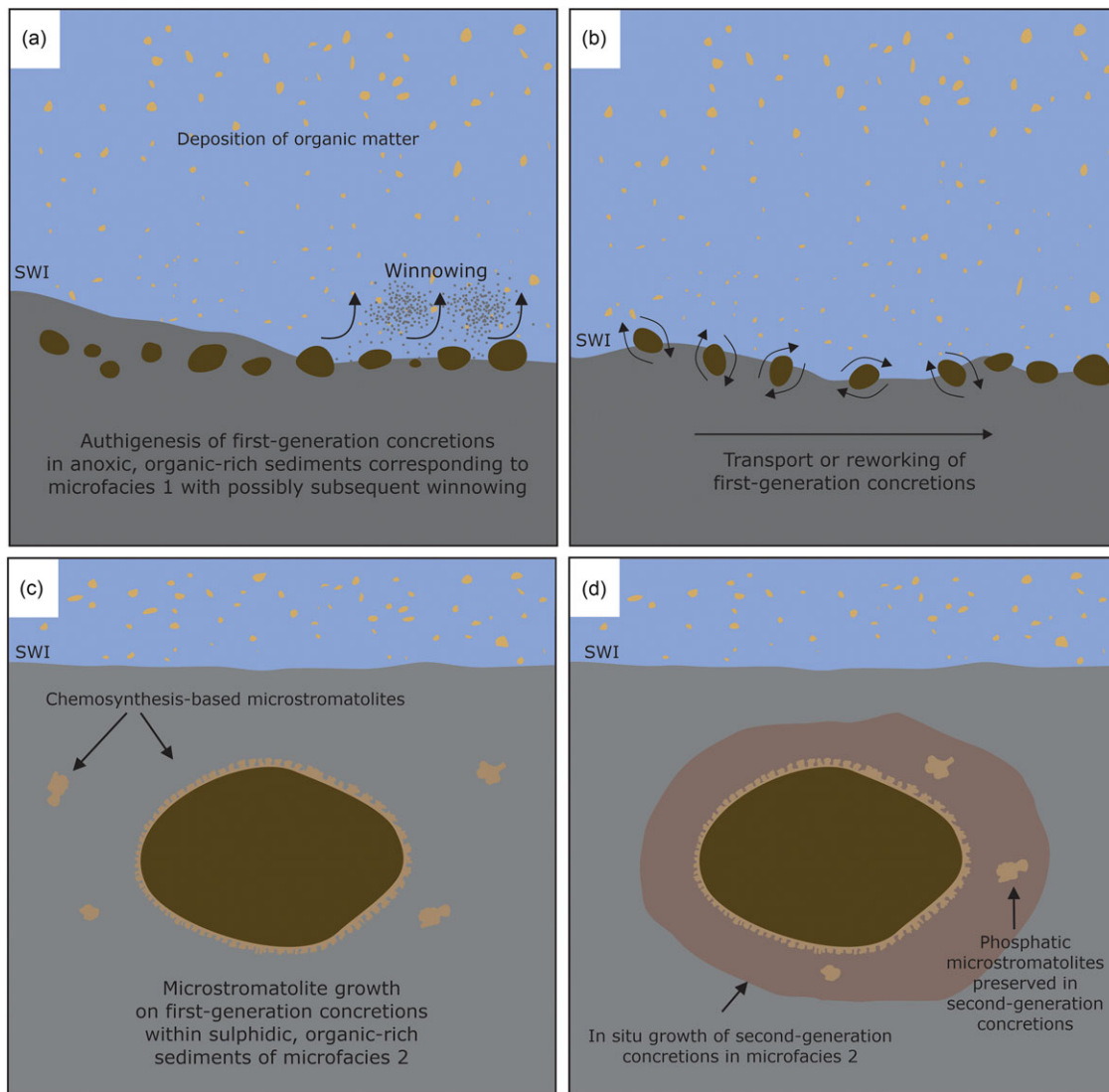
Figure 12. (Colour online) Schematic cartoon illustrating the formation of phosphatic concretions and phosphatic microstromatolites at Drewer, SWI = sediment–water interface. (a) Autochthonous formation of first-generation concretions in anoxic, organic-rich sediments. (b) Transport and redeposition of first-generation concretions. (c) Growth of phosphatic microstromatolites on first-generation concretions within sulphidic sediments. (d) Formation of second-generation concretions around first-generation concretions during sulphidic conditions in the sediment.

the phosphatic concretions and the microstromatolites formed within the sediments. The metabolic activity of sulphate-reducing bacteria gradually shifted the environmental conditions in the sediments from anoxic to sulphidic during a second phase of phosphatic concretion growth (Fig. 12d), as suggested by the occurrence of pyrite within the second-generation concretions (Fig. 8a, d).

6. Conclusions

The Lower Alum Shale Event is archived within black shales deposited at the base of the Carboniferous, cropping out in the Rhenish Massif at Drewer. These black shales are rich in phosphate minerals, specifically apatite, and contain abundant phosphatic concretions that grew in two generations under anoxic to sulphidic conditions within the sediments during a sea-level highstand. The phosphatic concretions also served as a substrate for phosphatic microstromatolites, which are present in various morphologies including branched and cauliflower-shaped types attached to the

first-generation concretions, as well as individual aggregates present within the second-generation concretions. Carbon stable isotope analyses of PAC derived from the phosphatic microstromatolites reveal low $\delta^{13}C$ values compared to dissolved inorganic carbon of Early Carboniferous seawater, possibly pointing to a chemotrophic metabolism of the mat-forming microorganisms. Together with the inferred environmental conditions during black shale deposition and the formation of phosphatic concretions, these results suggest that the stromatolite-forming microbial mats thrived in an aphotic environment. Stromatolites through Earth's history have mostly been interpreted as being the remnants of photosynthetic cyanobacteria, and therefore seen as indicators for shallow water environments. This study, however, shows that microbial communities forming stromatolites can also inhabit deep-water settings, and that the mat-forming microorganisms do not necessarily depend on photosynthesis as primary metabolic pathway. The reconstruction of environmental conditions and microbial metabolisms during stromatolite growth should

therefore always regard chemotrophy as a feasible alternative to the common interpretation of stromatolites formed by cyanobacteria in shallow water settings within the photic zone.

Competing interests. There is no conflict of interest to report.

References

Allwood AC, Walter MR, Burch IW and Kamber BZ (2007) 3.43 billion-year-old stromatolite reef from the Pilbara Craton of Western Australia: Ecosystem-scale insights to early life on earth. *Precambrian Research* **158**, 198–227.

Allwood AC, Walter, MR, Kamber BZ, Marshall CP and Burch IW (2006) Stromatolite reef from the early Archaean era of Australia. *Nature* **441**, 714–8.

Altenberger U, Besch T, Mocek B, Zaipeng Y and Yong S (1990) Geochemie und Geodynamik des Böllsteiner Odenwaldes. Mainz. *Geowissenschaftliche Mitteilungen* **19**, 183–200.

Arning ET, Birgel D, Brunner B and Peckmann J (2009b) Bacterial formation of phosphatic laminites off Peru. *Geobiology* **7**, 295–307.

Arning ET, Birgel D, Schulz-Vogt HN, Holmkvist L, Jørgensen BB, Larson A and Peckmann J (2008) Lipid biomarker patterns of phosphogenic sediments from upwelling regions. *Geomicrobiology Journal* **25**, 69–82.

Arning ET, Lückge, A, Breuer C, Gussone N, Birgel D and Peckmann J (2009a) Genesis of phosphorite crusts off Peru. *Marine Geology* **262**, 68–81.

Arthur MA and Sagemann BB (1994) Marine black shales: depositional mechanisms and environments of ancient deposits. *Annual Reviews in Earth and Planetary Sciences* **22**, 499–551.

Aufort J, Segalen L, Gervais C, Paulatto L, Blanchard M and Balan E (2017) Site-specific equilibrium isotopic fractionation of oxygen, carbon and calcium in apatite. *Geochimica et Cosmochimica Acta* **219**, 57–73.

Bailey JV, Corsetti FA, Greene SE, Crosby CH, Liu P and Orphan VJ (2013) Filamentous sulfur bacteria preserved in modern and ancient phosphatic sediments: implications for the role of oxygen and bacteria in phosphogenesis. *Geobiology* **11**, 397–405.

Bailey JV, Joye SB, Kalanetra KM, Flood BE and Corsetti FA (2007) Evidence of giant sulphur bacteria in Neoproterozoic phosphorites. *Nature* **445**, 198–201.

Banner JL and Hanson GN (1990) Calculation of simultaneous isotopic and trace element variations during water-rock interaction with applications to carbonate diagenesis. *Geochimica et Cosmochimica Acta* **54**, 3123–37.

Barnes BD, Husson JM and Peters SE (2020) Authigenic carbonate burial in the Late Devonian–early Mississippian Bakken Formation (Williston Basin, USA). *Sedimentology* **67**, 2065–94.

Becker G (1999) Verkieselte Ostracoden vom Thüringer Ökotyp aus den Devon/Karbon- Grenzschichten (Top Wocklumer Kalk und Basis Hangenberg-Kalk) im Steinbruch Drewer (Rheinisches Schiefergebirge). Die "natürliche" D/C-Grenze. *Courier Forschungsinstitut Senckenberg* **218**, 1–159.

Becker P, Libowitzky E, Kleinschrodt R and Bohatý L (2016) Linear optical properties and Raman spectroscopy of natural fluorapatite. *Crystal Research and Technology* **51**, 282–9.

Becker RT (1992) Analysis of ammonoid palaeobiogeography in relation to the global Hangenberg (Terminal Devonian) and Lower Alum Shale (Middle Tournaisian) events. *Annales de la Société géologique de Belgique* **115**, 459–73.

Becker RT, Hartenfels S and Kaiser SI (2021) Review of Devonian-Carboniferous boundary sections in the Rhenish Slate Mountains (Germany). *Palaeobiodiversity and Palaeoenvironments* **101**, 357–420.

Becker RT, Hartenfels S, Weyer D and Kumpan T (2016) The Famennian to lower Viséan at Drewer (northern Rhenish Massif). *Münstersche Forschungen zur Geologie und Paläontologie* **108**, 158–78.

Benitez-Nelson CA (2000) The biogeochemical cycling of phosphorus in marine systems. *Earth-Science Reviews* **51**, 109–35.

Berndmeyer C, Birgel D, Brunner B, Wehrmann LM, Jöns N, Bach W, Arning ET, Föllmi KB and Peckmann J (2012) The influence of bacterial activity on phosphorite formation in the Miocene Monterey formation, California. *Palaeogeography Palaeoclimatology Palaeoecology* **317–318**, 171–81.

Böhm F and Brachert TC (1993) Deep-water stromatolites and *Frutexites* Maslov from the Early and Middle Jurassic of S-Germany and Austria. *Facies* **28**, 145–68.

Bosak T, Liang B, Sim MS and Petroff AP (2009) Morphological record of oxygenic photosynthesis in conical stromatolites. *Proceedings of the National Academy of Sciences USA* **106**, 10939–43.

Böttcher ME, Gehlken P-L and Steele DF (1997) Characterization of inorganic and biogenic magnesian calcites by Fourier transform infrared spectroscopy. *Solid State Ionics* **101–103**, 1379–85.

Böttcher ME, Neubert N, Escher P, von Allmen K, Samankassou E and Nägler TF (2018) Multi-isotope (Ba, C, O) partitioning during experimental carbonatization of a hyperalkaline solution. *Geochemistry* **78**, 241–7.

Bradbury HJ, Vandeginste V and John CM (2015) Diagenesis of phosphatic hardgrounds in the Monterey formation: a perspective from bulk and clumped isotope geochemistry. *Geological Society of America Bulletin* **127**, 1453–63.

Brand U and Veizer J (1981) Chemical diagenesis of a multicomponent carbonate system — 2: stable isotopes. *Journal of Sedimentary Petrology* **51**, 987–97.

Brand WA and Coplen TB (2012) Stable isotope deltas: tiny, yet robust signatures in nature. *Isotopes in Environmental and Health Studies* **48**, 393–409.

Brinkmann R (1948) Die Mitteldeutsche Schwelle. *Geologische Rundschau* **36**, 56–66.

Brüchert V, Jørgensen BB, Neumann K, Riechmann D, Schlösser M and Schulz H (2003) Regulation of bacterial sulfate reduction and hydrogen sulfide fluxes in the central Namibian coastal upwelling zone. *Geochimica et Cosmochimica Acta* **67**, 4505–18.

Buggisch W and Joachimski MM (2006) Carbon isotope stratigraphy of the Devonian of Central and Southern Europe. *Palaeogeography Palaeoclimatology Palaeoecology* **240**, 68–88.

Buggisch W, Joachimski MM, Sevastopulo G and Morrow JR (2008) Mississippian $\delta^{13}C_{carb}$, and conodont apatite $\delta^{18}O$ records — their relation to the Late Palaeozoic Glaciation. *Palaeogeography Palaeoclimatology Palaeoecology* **268**, 273–92.

Büttner SH, Isemonger EC, Isaacs M, van Niekerk D, Sipler RE and Dorrington RA (2021) Living phosphatic stromatolites in a low-phosphorus environment: implications for the use of phosphorus as a proxy for phosphate levels in paleo-systems. *Geobiology* **19**, 35–47.

Caird RA, Pufahl PK, Hiatt EE, Abram MB, Rocha AJD and Kyser TK (2017) Ediacaran stromatolites and intertidal phosphorite of the Salitre Formation, Brazil: phosphogenesis during the Neoproterozoic Oxygenation event. *Sedimentary Geology* **350**, 55–71.

Clausen C-D, Leuteritz K and Ziegler W (1989) Ausgewählte Profile an der Devon/Karbon-Grenze im Sauerland (Rheinisches Schiefergebirge). *Fortschritte der Geologischen Rheinländischen Universität Westfalen* **35**, 161–226.

Cosmidis J, Benzerara K, Menguy N and Arning E (2013) Microscopy evidence of bacterial microfossils in phosphorite crusts of the Peruvian shelf: Implications for phosphogenesis mechanisms. *Chemical Geology* **359**, 10–22.

Crosby CH and Bailey JV (2012) The role of microbes in the formation of modern and ancient phosphatic mineral deposits. *Frontiers in Microbiology* **3**, article 241.

Crosby CH, Bailey JV and Sharma M (2014) Fossil evidence of iron-oxidizing chemolithotrophy linked to phosphogenesis in the wake of the Great Oxidation event. *Geology* **42**, 1015–8.

Czaja AD, Beukes NJ and Osterhout JT (2016) Sulfur-oxidizing bacteria prior to the Great Oxidation Event from the 2.52 Ga Gamohaan Formation of South Africa. *Geology* **44**, 983–6.

Dellwig O, Leipe T, März C, Glockzin M, Pollehne F, Schnetger B, Yakushev EV, Böttcher ME and Brumsack H-J (2010) A new particulate Mn-Fe-P shuttle at the redoxcline of anoxic basins. *Geochimica et Cosmochimica Acta* **74**, 7100–15.

Dombrowski A, Henjes-Kunst F, Höhndorf A, Kröner A, Okrusch M and Richter P (1995) Orthogneisses in the Spessart Crystalline complex, Northwest Bavaria: Silurian granitoid magmatism at an active continental margin *Geologische Rundschau* **84**, 399–411.

Downs RT (2006) The RRUFF Project: an integrated study of the chemistry, crystallography, Raman and infrared spectroscopy of minerals. *Program and Abstracts of the 19th General Meeting of the IMA in Kobe, Japan* O03-13.

Drummond JBR, Pufahl PK, Porto CG and Carvalho M (2015) Neoproterozoic peritidal phosphorite from the Sete Lagoas formation (Brazil) and the Precambrian phosphorus cycle. *Sedimentology* **62**, 1978–2008.

Dupraz C and Visscher P (2005) Microbial lithification in marine stromatolites and hypersaline mats. *Trends in Microbiology* **13**, 429–38.

Eckelmann K, Nesbor H-D, Königshof P, Linnemann U, Hofmann M, Lange J-M and Sagawe A (2014) Plate interactions of Laurussia and Gondwana during the formation of Pangaea — constraints from U–Pb LA–SF–ICP–MS detrital zircon ages of Devonian and early Carboniferous siliciclastics of the Rhenohercynian zone, Central European Variscides. *Gondwana Research* **25**, 1484–500.

Ferdelman TG, Fossing H and Neumann K (1999) Sulfate reduction in surface sediments of the southeast Atlantic continental margin between 15°38'S and 27°57'S (Angola and Namibia). *Limnolology and Oceanography* **44**, 650–61.

Filek T, Homayer F, Feichtinger I, Berning B, Pollerspöck J, Zwicker J, Smrzka D, Peckmann J, Kranner M, Mandic O, Reichenbacher B, Kroh A, Uchman A, Roetzel R and Harzhauser M (2021) Environmental conditions during the late Oligocene transgression in the North Alpine Foreland Basin (Eferding Formation, Egerian) – a multidisciplinary approach. *Palaeogeography Palaeoclimatology Palaeoecology* **580**, article 110527.

Filippelli GM (2011) Phosphate rock formation and marine phosphorus geochemistry: the deep time perspective. *Chemosphere* **84**, 759–66.

Filipelli GM and Delaney ML (1996) Phosphorus geochemistry of equatorial Pacific sediments. *Geochimica et Cosmochimica Acta* **60**, 1479–95.

Föllmi KB (1996) The phosphorus cycle, phosphogenesis, and marine phosphate-rich deposits. *Earth-Science Reviews* **40**, 55–124.

Froelich PN (1988) Kinetic control of dissolved phosphate in natural rivers and estuaries: a primer on the phosphate buffer mechanism. *Limnology and Oceanography* **33**, 649–68.

Ganai JA and Rashid SA (2019) Anoxia and fluctuating climate recorded from the Devonian–Carboniferous black shales, Tethys Himalaya, India: a multi-proxy approach. *International Journal of Earth Sciences* **108**, 863–83.

Gischler E, Fuchs A, Bach W and Reitner J (2021) Massive cryptic microbe-sponge deposits in a Devonian fore-reef slope (Elbingerode Reef Complex, Harz Mts., Germany). *PalZ* **95**, 683–707.

Glenn CR, Föllmi KB, Riggs SR, Baturin GN, Grimm KA, Trappe J, Abed AM, Galli-Oliver C, Garrison RE, Ilyin AV, Jehl C, Rohrlich V, Sadaqah RMY, Schildowski M, Sheldon RE and Siegmund H (1994) Phosphorus and phosphorites: sedimentology and environments of formation. *Eclogae Geolgica Helveticae* **87**, 747–88.

Goldhammer T, Brüchert V, Ferdelman TG and Zabel M (2010) Microbial sequestration of phosphorus in anoxic upwelling sediments. *Nature Geosciences* **3**, 557–61.

Harrick NJ (1967) *Internal Reflection Spectroscopy*. New York: Interscience Publication, Wiley, 327 p.

Heim C, Quéric N-V, Ionescu D, Schäfer N and Reitner J (2017) *Frutexites*-like structures formed by iron oxidizing biofilms in the continental subsurface (Äspö Hard Rock Laboratory, Sweden). *PLoS One* **12**, e0177542.

Heydari E, Wade WJ and Hassanzadeh J (2001) Diagenetic origin of carbon and oxygen isotope compositions of Perman – Triassic boundary strata. *Sedimentary Geology* **143**, 191–7.

Hofmann P (1997) Infrarotspektroskopische Untersuchungen der Hydroxid- und Carbonat-Ionen in natürlichen Apatiten. PhD Thesis, University of Karlsruhe.

Ingall E and Jahnke R (1994) Evidence for enhanced phosphorus regeneration from marine sediments overlain by oxygen depleted waters. *Geochimica et Cosmochimica Acta* **58**, 2571–5.

Jakubowicz M, Belka Z and Berkowski B (2014) *Frutexites* encrustations on rugose corals (Middle Devonian, southern Morocco): complex growth of microbial microstromatolites. *Facies* **60**, 631–50.

Jarosewich E, Nelen JA and Norberg JA (1980) Reference samples for electron microprobe analysis. *Geostandards Newsletter* **4.1**, 43–7.

Jenkyns HC (2010) Geochemistry of oceanic anoxic events. *Geochemistry Geophysics Geosystems* **11**, Q03004.

Jensen HS, Mortensen PB, Andersen FO, Rasmussen E and Jensen A (1995) Phosphorus cycling in a coastal marine sediment, Aarhus Bay, Denmark. *Limnology and Oceanography* **40**, 908–17.

Jørgensen, BB and Revsbach NP (1983) Colorless sulfur bacteria, *Beggiatoa* spp. and *Thiovulum* spp., in O_2 and H_2S microgradients. *Applied and Environmental Microbiology* **45**, 1261–70.

Kaiser SI, Aretz M and Becker RT (2015) The global Hangenberg Crisis (Devonian–Carboniferous transition): review of a first-order mass extinction. In *Devonian Climate, Sea Level and Evolutionary Events* (eds RT Becker, P Königshof and CE Brett), pp. 387–437. London: Geological Society of London, Special Publications no. 423.

Kaiser SI, Becker TR and El Hassani A (2007) Middle to Late Famennian successions at Ain Jemaa (Moroccan Meseta) implications for regional correlation, event stratigraphy and synsedimentary tectonics of NW Gondwana. *Geological Society of London Special Publication* **278**, 237–60.

Kaiser SI, Becker RT, Steuber T and Aboussalam SZ (2011) Climate-controlled mass extinctions, facies, and sea-level changes around the Devonian–Carboniferous boundary in the eastern Anti-Atlas (SE Morocco). *Palaeogeography Palaeoclimatology Palaeoecology* **310**, 340–64.

Kaiser SI, Steuber T and Becker RT (2008) Environmental change during the Late Famennian and Early Tournaisian (Late Devonian–Early Carboniferous): implications from stable isotopes and conodont biofacies in southern Europe. *Geological Journal* **43**, 241–60.

Kaiser SI, Steuber T, Becker RT and Joachimski MM (2006) Geochemical evidence for major environmental change at the Devonian–Carboniferous boundary in the Carnic Alps and the Rhenish Massif. *Palaeogeography Palaeoclimatology Palaeoecology* **240**, 146–60.

Kolodny Y and Kaplan IR (1970) Carbon and oxygen isotopes in apatite CO_2 and co-existing calcite from sedimentary phosphorite. *Journal of Sedimentary Petrolology* **40**, 954–9.

Komatsu T, Kato S, Hirata K, Takashima R, Ogata Y, Oba M, Naruse H, Ta PH, Nguyen PD, Dang HT, Doan TN, Nguyen HH, Sakata S, Kaiho K and Königshof P (2014) Devonian–Carboniferous transition containing a Hangenberg Black Shale equivalent in the Pho Han Formation on Cat Ba Island, northeastern Vietnam. *Palaeogeography Palaeoclimatology Palaeoecology* **404**, 30–43.

Königshof P, Becker RT and Hartenfels S (2016) The Rhenish Massif as a part of the European Variscides. *Münstersche Forschungen zur Geologie und Paläontologie* **108**, 1–13.

Korn D (2010) Lithostratigraphy and biostratigraphy of the Kulm succession in the Rhenish Mountains. *Zeitschrift der Deutschen Gesellschaft der Geowissenschaften* **161**, 431–53.

Korn D, Clausen C-D, Belka Z, Leuteritz K, Luppold FW, Feist R and Weyer D (1994) Die Devon/Karbon-Grenze bei Drewer (Rheinisches Schiefergebirge). *Geologische Paläontologische Westfalen* **29**, 97–147.

Kossmat F (1927) Die tektonische Stellung des Gebiets von Elbingerode. *Zeitschrift der Deutschen Geologischen Gesellschaft* **79**, 177.

Kraal P, Slomp CP, Reed DC, Reichart G-J and Poulton SW (2012) Sedimentary phosphorus and iron cycling in and below the oxygen minimum zone of the northern Arabian Sea. *Biogeosciences* **9**, 2603–24.

Krajewski KP, Lesniak PM, Lacka B and Zawidzki P (2000) Origin of phosphatic stromatolites in the Upper Cretaceous condensed sequence of the Polish Jura Chain. *Sedimentary Geology* **136**, 89–112.

Kumpan T, Babek O, Kalvoda J, Grygar TM, Fryda J, Becker RT and Hartenfels S (2015) Petrophysical and geochemical signature of the Hangenberg events: an integrated stratigraphy of the Devonian–Carboniferous boundary interval in the Northern Rhenish Massif (Avalonia, Germany). *Bulletin of Geosciences* **90**, 667–94.

Kumpan T, Babek O, Kalvoda J, Matys Grygar T, Fryda J (2014) Sea-level and environmental changes around the Devonian–Carboniferous boundary in the Namur–Dinant Basin (S Belgium, NE France): a multi-proxy stratigraphic analysis of carbonate ramp archives and its use in regional and interregional correlations. *Sedimentary Geology* **311**, 43–59.

Küster-Heins K, Steinmetz E, De Lange GJ and Zabel M (2010) Phosphorus cycling in marine sediments from the continental margin off Namibia. *Marine Geology* **274**, 95–106.

Lafuente B, Downs RT, Yang H and Stone N (2015) The power of databases: the RRUFF project. In *Highlights in Mineralogical Crystallography* (eds T Armbruster and RM Danisi), pp. 1–30. Berlin, Germany: W. De Gruyter.

Laws EA, Popp BN, Bidigare RR, Kennicutt MC and Macko SA (1995) Dependence of phytoplankton carbon isotopic composition on growth rate and $[CO_2]_{aq}$: theoretical considerations and experimental results. *Geochimica et Cosmochimica Acta* **59**, 1131–8.

Lazar I, Gradinaru M and Petrescu L (2013) Ferruginous microstromatolites related to Middle Jurassic condensed sequences and hardgrounds (Bucegi Mountains, Southern Carpathians, Romania). *Facies* **59**, 359–90.

Lepland A, Joosu L, Kirsimäe K, Prave AR, Romashkin AE, Crne AE, Martin AP, Fallick AE, Somelar P, Ürpraus K, Mänd K, Roberts NMW, van Zuilen MA, Wirth R and Schreiber A (2013) Potential influence of sulphur bacteria on Palaeoproterozoic phosphogenesis. *Nature Geoscience* **7**, 20–4.

Loeffler N, Fiebig J, Mulch A., Tütken T, Schmitt BC, Bajnai D, Conrad AC, Wacker U and Böttcher M (2019) Refining the temperature dependence of the oxygen and clumped isotopic compositions of structurally bound carbonate in apatite. *Geochimica et Cosmochimica Acta* **253**, 19–38.

Lomnitz U, Sommer S, Dale AW, Löscher CR, Noffke A, Wallmann K and Hensen C (2016) Benthic phosphorus cycling in the Peruvian oxygen minimum zone. *Biogeosciences* **13**, 1367–86.

Lu M, Lu Y, Ikejiri T, Hogancamp N, Sun Y, Wu Q, Carroll R, Cemen I and Pashin J (2019) Geochemical evidence of first forestation in the southernmost Euramerica from Upper Devonian (Famennian) black shales. *Scientific Reports* **9**, article 7581.

Lundberg J and McFarlane DA (2011) Subaerial freshwater phosphatic stromatolites in Deer Cave, Sarawak — a unique geobiological cave formation. *Geomorphology* **128**, 57–72.

Luppold FW, Clausen C-D, Korn D and Stoppel D (1994) Devon/Karbon-Grenzprofile im Bereich von Remscheid-Altenaer Sattel, Warsteiner Sattel, Briloner Sattel und Attendorn-Elsper Doppelmulde (Rheinisches Schiefergebirge). *Geologische Paläontologische Westfalen* **29**, 7–69.

Martinez AM, Boyer DL, Droser ML, Barrie C and Love GD (2019) A stable and productive marine microbial community was sustained through the end-Devonian Hangenberg Crisis within the Cleveland Shale of the Appalachian Basin, United States. *Geobiology* **17**, 27–42.

März C, Poulton SW, Beckmann B, Küster K, Wagner T and Kasten S (2008) Redox sensitivity of P cycling during marine black shale formation: dynamics of sulfidic and anoxic, non-sulfidic bottom waters. *Geochimica et Cosmochimica Acta* **72**, 3703–17.

Myrow PM, Strauss JV, Creveling JR, Sicard KR, Ripperdan R, Sandberg CA and Hartenfels S (2011) A carbon isotopic and sedimentological record of the latest Devonian (Famennian) from the Western U.S. and Germany. *Palaeogeography Palaeoclimatology Palaeoecology* **306**, 147–59.

O'Leary MH (1988) Carbon isotopes in photosynthesis. *BioScience* **38**, 328–36.

O'Neil JR, Clayton RN and Mayeda TK (1969) Oxygen isotope fractionation in divalent metal carbonates. *Journal of Chemical Physics* **51**, 5547–58.

Oncken O, Plesch A, Weber K, Ricken W and Schrader S (2000) Passive margin detachment during arc-continent collision (Central European Variscides). In *Orogenic Processes: Quantification and Modelling in the Variscan Belt* (eds W Franke, V Haak, O Oncken and D Tanner), pp. 199–216. London: Geological Society of London, Special Publication no. 179.

Oncken O, von Winterfeld C and Dittmar U (1999) Accretion of a rifted passive margin: the Late Paleozoic Rhenohercynian fold and thrust belt (Middle European Variscides). *Tectonics* **18**, 75–91.

Oncken O and Weber K (1995) The structure of the Rhenohercynian. In *Tectonostratigraphic Evolution of the Central and East European orogens* (eds RD Dallmeyer, W Franke and K Weber), pp. 50–8. Berlin Heidelberg: Springer.

Paschall OC, Carmichael SK, Königshof P, Waters JA, Ta Hoa P, Komatsu T and Dombrowski AD (2019) The Hangenberg Event in Vietnam: sustained ocean anoxia with a volcanic trigger? *Global and Planetary Change* **175**, 64–81.

Penel G, Leroy G, Rey C, Sombret B, Huvenne JP and Bres E (1997) Infrared and Raman microspectrometry study of fluor-fluor-hydroxy and hydroxyapatite powders. *Journal of Material Science: Materials in Medicine* **8**, 271–7.

Qie W, Liu J, Wang X, Mii H-S, Zhang X, Huang X, Yao L, Algeo TJ and Luo G (2015) A carbon isotopic and sedimentological record of the latest Devonian (Famennian) from the Western U.S. and Germany. *Palaeogeography Palaeoclimatology Palaeoecology* **418**, 290–303.

Rakocinski M, Ksiazak D, Pisarzowska A, Zaton M and Aretz M (2023) Weak and intermittent anoxia during the mid-Tournaisian (Mississippian) anoxic event in the Montagne Noire, France. *Geological Magazine* **160**, 831–54.

Rakocinski M, Marynowski L, Zaton M and Filipak P (2021) The mid-Tournaisian (Early Carboniferous) anoxic event in the Laurussian shelf basin (Poland): an integrative approach. *Palaeogeography Palaeoclimatology Palaeoecology* **566**, 110236.

Rao VP, Michard A, Naqvi SWA, Böttcher ME, Krishnawamy R, Thamban R, Natarajan R and Borole DV (2002) Quaternary phosphorites off the southeast coast of India. *Chemical Geology* **182**, 483–502.

Rao VP, Rao M and Raju DSN (2000) Quaternary phosphorites from the continental margin off Chennai, southeast India: analogs of ancient phosphate stromatolites. *Journal of Sedimentary Research* **70**, 1197–209.

Reitner J, Peckmann J, Blumenberg M, Michaelis W, Reimer A and Thiel V (2005) Concretionary methane-seep carbonates and associated microbial communities in Black Sea sediments. *Palaeogeography Palaeoclimatology Palaeoecology* **227**, 18–30.

Reitner J, Wilmsen M and Neuweiler F (1995) Cenomanian/Turonian sponge microbialite deep-water hardground community (Liencres, Northern Spain). *Facies* **32**, 203–12.

Rickard DT (2021) *Framboids*. New York: Oxford University Press.

Ruttenberg KC and Berner RA (1993) Authigenic apatite formation and burial in sediments from non-upwelling, continental margin environments. *Geochimica et Cosmochimica Acta* **57**, 991–1007.

Sagemann BB, Murphy AE, Werne JP, Ver Straeten CA, Hollander DJ and Lyons TW (2003) A tale of shales: the relative roles of production, decomposition, and dilution in the accumulation of organic-rich strata, Middle–Upper Devonian, Appalachian basin. *Chemical Geology* **195**, 229–73.

Sallstedt T, Bengston S, Broman C, Crill PM and Canfield DE (2018) Evidence of oxygenic phototrophy in ancient phosphatic stromatolites from the Paleoproterozoic Vindhyan and Aravalli Supergroups, India. *Geobiology* **16**, 139–59.

Saltzman MR, Groessens E and Zhuravlev AV (2004) Carbon cycle models based on extreme changes in δ^{13}C: an example from the lower Mississippian. *Palaeogeography, Palaeoclimatology, Palaeoecology* **213**, 359–77.

Scasso RA and Castro LA (1999) Cenozoic phosphatic deposits in North Patagonia, Argentina: phosphogenesis, sequence-stratigraphy and paleoceanography. *Journal of South American Earth Sciences* **12**, 471–87.

Schenau SJ, Slomp CP and De Lange GJ (2000) Phosphogenesis and active phosphorite formation in sediments from the Arabian Sea oxygen minimum zone. *Marine Geology* **169**, 1–20.

Schlanger SO and Jenkyns HC (1976) Cretaceous Oceanic anoxic events: causes and consequences. *Geologie Mijnbouw* **55**, 179–84.

Schulz HN and Schulz HD (2005) Large sulfur bacteria and the formation of phosphorite. *Science* **307**, 416–8.

Siegmund H, Trappe J and Oschmann W (2002) Sequence stratigraphic and genetic aspects of the Tournaisian "Liegender Alaunschiefer" and adjacent beds. *International Journal of Earth Science* **91**, 934–49.

Sievert SM, Keine RP and Schultz-Vogt HN (2007) The sulfur cycle. *Oceanography* **20**, 117–23.

Smith CR, Glover AG, Treude T, Higgs ND and Amon DJ (2015) Whale-fall ecosystems: recent insights into ecology, paleoecology, and evolution. *Annual Review of Marine Science* **7**, 571–96.

Sobolev DB, Zhuravlev AV and Tsyganko VS (2000) Stop 8. Upper Devonian–Lower Carboniferous succession on the Kozhym River. *Ichthyolith Issue Special Publications* **6**, Suppl, 101–11.

Soudry D (2000) Microbial phosphate sediment. In *Microbial Sediments* (eds RE Riding and SM Awramik), pp. 127–36. Berlin Heidelberg: Springer-Verlag.

Spalletta C, Corradini C, Feist R, Korn D, Kumpan T, Perri MC, Pondrelli M and Venturini C (2021) The Devonian–Carboniferous boundary in the Carnic Alps (Austria and Italy). *Palaeobiodiversity and Palaeoenvironments* **101**, 487–505.

Stal LJ (2012) Cyanobacterial mats and stromatolites. In *Ecology of Cyanobacteria II: Their Diversity in Space and Time* (ed BA Whitton), pp. 65–125. Berlin Heidelberg.

Thamdrup B and Canfield DE (1996) Pathways of carbon oxidation in continental margin sediments off central Chile. *Limnology and Oceanography* **41**, 1629–50.

Tong H, Wang Q, Peckmann J, Cao Y, Chen L, Zhou W and Chen D (2016) Diagenetic alteration affecting $\delta^{18}O$, $\delta^{13}C$ and $^{87}Sr/^{86}Sr$ signatures of carbonates: a case study on Cretaceous seep deposits from Yarlung-Zangbo Suture Zone, Tibet, China. *Chemical Geology* **444**, 71–82.

Ullmann CV, Thibault N, Ruhl M, Hesselbo SP and Korte C (2014) Effect of a Jurassic oceanic anoxic event on belemnite ecology and evolution. *Proceedings of the National Academy of Sciences USA* **111**, 10073–6.

von Raumer JF, Nesbor H-D and Stampfli GM (2017) The north-subducting Rheic Ocean during the Devonian: consequences for the Rhenohercynian ore sites. *International Journal of Earth Science* **106**, 2279–96.

von Raumer JF and Stampfli H-D (2008) The birth of the Rheic Ocean — Early Palaeozoic subsidence patterns and subsequent tectonic plate scenarios. *Tectonophysics* **461**, 9–20.

Walliser OH (1996) Global events in the Devonian and Carboniferous. *In: Global Events and Event Stratigraphy in the Phanerozoic* (ed OH Walliser), pp. 225–50. Berlin Heidelberg: Springer.

White WB (1974) The carbonate minerals. In *Infrared Spectra of Minerals* (ed VC Farmer), pp. 227–84. Twickenham, Middlesex: Mineralogical Society Monograph 4.

Wilkin RT, Barnes HL and Brantley SL (1996) The size distribution of framboidal pyrite in modern sediments: an indicator of redox conditions. *Geochimica et Cosmochimica Acta* **60**, 3897–912.

Williams LA and Reimers C (1983) Role of bacterial mats in oxygen-deficient marine basins and coastal upwelling regimes: preliminary report. *Geology* **11**, 267–9.

Woods AD and Baud A (2008) Anachronistic facies from a drowned Lower Triassic carbonate platform: lower member of the Alwa Formation (Ba'id Exotic), Oman Mountains. *Sedimentary Geology* **209**, 1–14.

Zachos JC, Schoutefn S, Bohaty S, Sluijs A, Brinkhuis H, Gibbs S, Bralower T and Quattlebaum T (2006) Extreme warming of mid-latitude coastal ocean during the Paleocene–Eocene thermal maximum: inferences from TEX_{86} and isotope data. *Geology* **34**, 737–40.

Zeh A and Gerdes A (2010) Baltica- and Gondwana-derived sediments in the Mid-German Crystalline Rise (Central Europe): implications for the closure of the Rheic ocean. *Gondwana Research* **17**, 254–63.

Zhang M, Becker RT, Ma X, Zhang Y and Zong P (2019) Hangenberg Black Shale with cymaclymeniid ammonoids in the terminal Devonian of South China. *Palaeobiodiversity and Palaeoenvironments* **99**, 129–42.

Zheng Y-F (2016) Oxygen isotope fractionation in phosphates: the role of dissolved complex anions in isotope exchange. *Isotopes in Environmental and Health Studies* **52**, 47–60.

Zopfi J, Böttcher ME and Jørgensen BB (2008) Biogeochemistry of sulfur and iron in *Thioploca*-colonized surface sediments in the upwelling area off central Chile. *Geochimica et Cosmochimica Acta* **72**, 827–43.

Zoss R, Ferrer FM, Flood BE, Jones DS, Louw DC and Bailey J (2019) Microbial communities associated with phosphogenic sediments and phosphoclast-associated DNA of the Benguela upwelling system. *Geobiology* **17**, 76–90.

Zwicker J, Smrzka D, Steindl F, Böttcher ME, Libowitzky E, Kiel S and Peckmann J (2021) Mineral authigenesis within chemosynthetic microbial mats: coated grain formation and phosphogenesis at a Cretaceous hydrocarbon seep, New Zealand. *The Depositional Record* **7**, 294–310.